J. Fluid Mech. (2006), *vol.* 548, *pp.* 165–196.
doi:10.1017/S0022112005007524 Printed in the United Kingdom

Instability mechanisms of a two-dimensional progressive internal gravity wave

By C. R. KOUDELLA[1]† AND C. STAQUET[2]‡

[1]Department of Applied Mathematics and Theoretical Physics, University of Cambridge, Centre for Mathematical Sciences, Wilberforce Road, Cambridge, CB3 OWA, UK

[2]Laboratoire des Ecoulements Géophysiques et Industriels, BP 53, 38041 Grenoble cedex 9, France

(Received 4 May 2005 and in revised form 21 July 2005)

We present a detailed investigation of the parametric subharmonic resonance mechanism that leads a plane, monochromatic, small-amplitude internal gravity wave, also referred to as the primary wave, to instability. Resonant wave interaction theory is used to derive a simple kinematic model for the parametrically forced perturbation, and direct numerical simulations of the Boussinesq equations in a vertical plane permit the nonlinear simulation of the internal gravity wave field. The processes that eventually drive the wave field to breaking are also addressed.

We show that parametric instability may be viewed as an optimized scenario for drawing energy from the primary wave, that is, from a periodic flow with both oscillating shear and density gradient. Optimal energy exchange maximizing perturbation growth is realized when the perturbation has a definite spatio-temporal structure: its energy is phase-locked with the vorticity of the primary wave. This organization allows the perturbation energy to alternate between kinetic form when locally the primary wave shear is negative, then maximizing kinetic energy extraction from the primary wave, and potential form when the primary wave shear is positive, then minimizing the reverse transfer to that wave. The perturbation potential energy increases through the primary wave density gradient whether the latter is positive, that is when the medium is of reduced static stability, or negative (increased static stability). When the primary wave amplitude is small, all energy transfer terms are predicted well by the kinematic model. One important result is that the rate of potential energy transfer from the primary wave to the perturbation is always larger than the rate of kinetic energy transfer, whatever the primary wave.

As the perturbation amplifies, overturned isopycnals first appear in reduced static stability regions, implying that the total field should become unstable through a buoyancy induced (or Rayleigh–Taylor) instability. Hence, a two-dimensional model is no longer valid for studying the subsequent flow development.

1. Introduction

A plane, linear, monochromatic internal gravity wave – termed the primary wave – in an inviscid stably stratified fluid under the Boussinesq approximation is unstable to infinitesimal perturbations. This was first shown by resonant wave interaction theory for weak steepness waves, i.e. $s \ll 1$ (Phillips 1966; Thorpe 1966; Hasselmann

† Present address: 404 1/2 Henry Street, Brooklyn, NY 11201, USA
‡ Author to whom correspondence should be addressed: Chantal.Staquet@hmg.inpg.fr.

1967) and subsequently by linear stability analysis for arbitrary steepness waves. When the primary wave steepness is smaller than 1 (i.e. the isopycnals are not overturned), a stability analysis of two-dimensional perturbations can be conducted (Mied 1976; Klostermeyer 1982), which reduces to resonant interaction theory in the limit of vanishing primary wave steepness (Drazin 1977). When the primary wave steepness is larger than 1 (the isopycnals are locally overturned), a stability analysis of three-dimensional perturbations has to be conducted in order to capture the most amplified modes (Klostermeyer 1991; Lombard & Riley 1996*a*; Sonmor & Klaassen 1997; see Staquet & Sommeria 2002 for a review). The main result of the linear stability analysis is that an internal gravity wave is unstable however large the associated Richardson number (this parameter is a measure of the stabilizing effect of the background stratification relative to the destabilizing effect of the vertical wave shear). For small-scale perturbations, the instability is of the parametric sub-harmonic type. The first experimental evidence was provided by Davis & Acrivos (1967) for gravity waves propagating at a thin density interface and by Martin, Simmons & Wunsch (1972) for waves propagating in a long channel uniformly stratified with salt water (see Phillips 1981 for a review). The parametric instability mechanism in a stratified fluid has received new theoretical interest when forcing occurs via a time-oscillating non-parallel velocity field (Majda & Shefter 1998, Leblanc 2003). Majda & Shefter (2003) thus showed that the dominant instability is a purely two-dimensional parametric instability whatever the stratification level, in agreement with the results of linear stability analysis for an internal gravity wave of steepness $s < 1$.

In the present paper, we investigate the mechanisms that lead a monochromatic progressive internal gravity wave of small steepness to instability. As attested by the references cited above, much attention has been given to this academic problem but, to our knowledge, the energy exchange process between the primary wave and the perturbation, and the subsequent nonlinear development of the perturbation have not been addressed in detail. This is the purpose of the present paper. We show that parametric instability may be viewed as an optimized scenario for drawing energy from the primary wave and that the amplified perturbation eventually destabilizes the whole wave field through a buoyancy-induced (or Rayleigh–Taylor) instability. Hence, a two-dimensional approach cannot be pursued further to study the subsequent flow development.

The study of nonlinear dynamical processes among internal gravity waves relies traditionally on laboratory experiments and on numerical simulations, and to a lesser extent on field observations (e.g. Thorpe 1966). Laboratory experiments usually involve standing waves (McEwan 1971; McEwan, Mander & Smith 1972; McEwan & Robinson 1975; Benielli & Sommeria 1998) or partially standing waves (Martin *et al.* 1972; Teoh, Ivey & Imberyer 1997), which are easier to generate in laboratory installations than progressive waves. In most numerical works reported in the literature, the statistical properties of a deterministic or of a random internal wave field are investigated in a vertical plane (for instance Orlanski & Cerasoli 1981; Frederiksen & Bell 1983, 1984; Chen & Holloway 1986). In Carnevale & Martin (1982) and Holloway (1979), these properties are compared to a statistical model (a review was made by Muller *et al.* 1986). Owing to the availability of high performance computers, recent numerical works have been able to address deterministic processes in both two and three dimensions. Lombard & Riley thus performed two- and three-dimensional numerical simulations of an unstable monochromatic progressive primary wave (Lombard & Riley 1996*b*), thereby complementing a linear stability analysis of this wave against three-dimensional perturbations (Lombard & Riley 1996*a*).

Bouruet-Aubertot, Sommeria & Staquet (1995) investigated the parametric instability mechanism of the standing primary wave analogue to the progressive primary wave that we consider in the present paper. As in Bouruet-Aubertot *et al.* (1995), we use resonant interaction theory to determine the most unstable resonant triads that govern the parametric instability growth; the novelty of the present work lies in a detailed analysis (i) of the energetics of the instability mechanisms, using two-dimensional numerical simulations and a simple kinematic model of the parametrically amplified perturbation, and (ii) of the nonlinear development of the perturbation field.

We shall assume that the primary wave propagates in a homogeneous medium at rest so that it will not be refracted by a spatially varying stratification or mean flow (see for instance Sutherland 1999, 2000 for the latter problem). The effect of the Earth's rotation, through the Coriolis force, will also be ignored (we refer to Miyazaki & Adachi 1998*a*, *b* and Lelong & Dunkerton 1998*a*, *b* for this subject).

The outline of the paper is as follows. In § 2, we present the equations of motion and describe the numerical model. Section 3 is devoted to a brief description of the overall behaviour of the wave field. The detailed investigation of the instability processes is addressed from § 4 onwords. In § 4, the parametric instability is studied in Fourier space, using resonant interaction theory; we show that the perturbation growth is controlled by a few resonant triads, which may be assumed to evolve independently during the early stage of the wave-field evolution. This permits us to derive a simple kinematic model, that relies upon one resonant triad only, to address the parametric instability process (§ 5). The energetics of the latter process are investigated in physical space in § 6. The instability mechanisms eventually leading the whole wave field to breakdown are addressed in § 7 and conclusions are drawn in a final section.

2. Equations of motion and numerical model

We consider the dynamics of a Newtonian fluid in a Cartesian coordinate frame $\boldsymbol{x} = x\boldsymbol{e}_x + y\boldsymbol{e}_y + z\boldsymbol{e}_z$ subject to a constant gravitational field $\boldsymbol{g} = -g\boldsymbol{e}_z$. The fluid is linearly stratified and its dynamics are governed by the Navier–Stokes equations in the Boussinesq approximation (see e.g. Cushman-Roisin 1994). The velocity field $\boldsymbol{u} = (u, v, w)$ is assumed to be incompressible, i.e. $\nabla \cdot \boldsymbol{u} = 0$. The pressure and density fields are split into hydrostatically balanced parts (p_0 and $\rho_0 + \bar{\rho}$) and fluctuating ($\tilde{p}$ and $\tilde{\rho}$) parts such that $p = p_0(z) + \tilde{p}(x, y, z, t)$ and $\rho = \rho_0 + \bar{\rho}(z) + \tilde{\rho}(x, y, z, t)$, respectively; ρ_0 is a constant reference density and $\bar{\rho}(z)$ is the initial background density profile, assumed to be linear. The hydrostatic density field sets the Brunt–Väisälä frequency, whose square is defined by $N^2 = -((g/\rho_0)(\mathrm{d}\bar{\rho}/\mathrm{d}z))$; N is therefore constant in our study.

Hereinafter, we assume two-dimensional fluid dynamics in the vertical (x, z)-plane. Incompressibility is satisfied by introducing the streamfunction $\psi(x, z, t)$ such that $u = \partial\psi/\partial z$, $w = -\partial\psi/\partial x$ and $\zeta = \nabla^2\psi$, where ζ denotes the two-dimensional vorticity scalar field. The Navier–Stokes equations in the Boussinesq approximation in terms of the streamfunction and fluctuating density fields are

$$\frac{\partial \nabla^2\psi}{\partial t} + J(\nabla^2\psi, \psi) = \frac{\partial \rho'}{\partial x} + \nu\nabla^4\psi, \tag{1}$$

$$\frac{\partial \rho'}{\partial t} + J(\rho', \psi) = -N^2\frac{\partial \psi}{\partial x} + \frac{\nu}{Pr}\nabla^2\rho'. \tag{2}$$

As is customary, we have introduced the reduced density fluctuations $\rho' = (g/\rho_0)\,\tilde{\rho}$ in order for the Brunt–Väisälä frequency to appear in equation (2). ν is the kinematic

viscosity and Pr is the Prandtl number. $J(A, B) = (\partial A/\partial x)(\partial B/\partial z) - (\partial A/\partial z)(\partial B/\partial x)$ is the Jacobian operator.

The computational domain is a square of side length 2π, and periodic boundary conditions are applied to the flow fields. Equations (1) and (2) may thus be integrated using a standard pseudospectral collocation method (e.g. Canuto *et al.* 1988) whereby the equations of motion are solved in Fourier space. The nonlinear terms give rise to the computation of convolution sums in Fourier space which are evaluated more cheaply in physical space instead, but at the expense of generating aliasing errors. These are eliminated with the help of a standard truncation method of the Fourier coefficients. The equations of motion are integrated in time using an explicit third-order Adams–Bashforth scheme. Molecular effects are modelled by a Laplacian operator with constant coefficients (ν and ν/Pr) implying that the reported simulations are direct numerical simulations (DNS). The Prandtl number is constant in our simulations and the kinematic viscosity is adjusted using the balance of energy. A numerical simulation is validated when this balance is satisfied to within a 1 % error at most. The largest (1 %) error occurs during wave breaking, that is when the flow is strongly nonlinear.

The initial condition of the computations is a plane, monochromatic, large-scale (relative to the domain side) internal gravity wave, termed the primary wave. Let $\boldsymbol{k} = (k, m)$ and ω denote the wave vector and frequency of the wave, respectively. The linear dispersion relation sets the dependency of ω upon $\boldsymbol{k}$:

$$\omega^2 = N^2 \cos^2\theta = N^2 \left(\frac{k}{\kappa}\right)^2, \tag{3}$$

where θ is the angle between the wave vector and the horizontal and $\kappa = \sqrt{k^2 + m^2}$ is the wave vector modulus. We shall use the convention that frequencies are positive (except in § 4). The linear polarization relations for such waves are thus given by (see Gill 1982 for instance)

$$\psi(x, z, t) = A \sin(\boldsymbol{k}\cdot\boldsymbol{x} - \omega t), \quad \rho'(x, z, t) = sg(k) A N \kappa \sin(\boldsymbol{k}\cdot\boldsymbol{x} - \omega t), \tag{4}$$

where A is the streamfunction amplitude of the wave; the coefficient $sg(k)$ is the sign of k and results from the positive frequency convention.

The steepness $s = u_{max}/c_x$ provides a non-dimensional measure of the wave amplitude and has the useful physical meaning that isopycnals are locally vertical when $s = 1$; u_{max} is the maximum wave-induced velocity along the x, say, horizontal direction and c_x is the phase velocity of the wave along that same direction. For the monochromatic wave (4), the steepness is expressed as

$$s = \frac{Am\kappa}{N}. \tag{5}$$

A non-dimensional measure of the wave amplitude is also provided by the Foude number $Fr = U/NL$, where U and L are a typical wave-induced velocity and length scale, respectively. Taking $U = A\kappa$ and $L = 1/\kappa$, Fr and s are simply related by $Fr = (\kappa/m)s$ for the monochromatic wave (4).

Since the plane wave (4) is a solution of the fully nonlinear equations of motion, (1)–(2), it is perturbed at initial time by a random noise in order to trigger instability. The noise spectrum is normalized such that the total perturbation energy is 10 orders of magnitude smaller than the primary wave energy.

Table 1 recapitulates the physical and numerical parameters used in the simulations. Primary wave attributes are denoted in the following by a 0 index, e.g. s_0. The main feature is that $\boldsymbol{k}_0 = (1, 1)$ in all DNS reported, so that $\theta_0 = 45°$. Since we shall

Run	A_0	s_0	ν	Δt
0	0.064	0.09	3.75×10^{-5}	0.016
1	0.128	0.18	0.75×10^{-4}	0.008
2	0.256	0.36	1.5×10^{-4}	0.004
3	0.5	0.71	3.0×10^{-4}	0.002

TABLE 1. Numerical and physical parameters of the simulations. A_0 is the initial amplitude of the streamfunction of the primary wave and s_0, defined by (5), is the steepness associated with the primary wave. ν is the kinematic viscosity and Δt is the time step. For all runs, the wave vector of the primary wave $\boldsymbol{k}_0$ is equal to (1, 1), the Brunt–Väisälä frequency N and the Prandtl number have a value of 1 and the resolution is (512, 512).

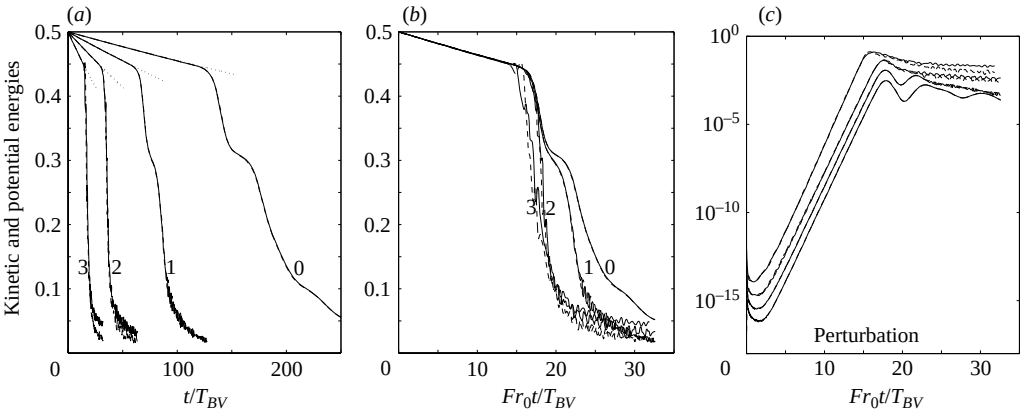

FIGURE 1. (a, b) Domain-averaged kinetic energy $\langle \mathrm{KE} \rangle$ (full line) and potential energy $\langle \mathrm{PE} \rangle$ (dashed line) of the flow normalized by the total (kinetic + potential) energy at $t = 0$ versus time (in Brunt–Väisälä periods) for all runs; the run number is indicated. The decay of the primary wave energy owing to molecular effects only is plotted using a dotted line. In (b), $\langle \mathrm{KE} \rangle$ and $\langle \mathrm{PE} \rangle$ are plotted versus time scaled by the Froude number of the primary wave Fr_0. (c) Domain-averaged kinetic energy $\langle \mathrm{KE}' \rangle$ and potential energy $\langle \mathrm{PE}' \rangle$ of the perturbation for the four runs, versus time scaled by Fr_0 (the energy level increases with the run number at a given time).

investigate the energetics of the parametric instability using resonant interaction theory, we shall consider a weak steepness primary wave. This is run 0 in the table. We shall also investigate the influence of a finite steepness on the instability and this is why s_0 is varied from 0.09 to 0.71. Since the spatial resolution of all DNS is the same, the time step and the viscosity are varied in accordance with changes in A_0 in order to satisfy the Courant criterion and the energy balance mentioned above. Most of our results are presented in units of time normalized by the Brunt–Väisälä period $T_{BV} = 2\pi/N$, also referred to as BVP.

3. Overall energetics of the wave field

The temporal evolution of the domain averaged kinetic and potential energy of the flow per unit mass, $\langle \mathrm{KE} \rangle = \langle (u^2 + w^2)/2 \rangle$ and $\langle \mathrm{PE} \rangle = \langle (\rho'/N)^2/2 \rangle$, respectively, are displayed in figures 1(a) and 1(b) for all runs. A domain average is denoted as $\langle\ \rangle$ throughout the paper. Figure 1(c) displays the domain averaged kinetic and potential energy of the perturbation, $\langle \mathrm{KE}' \rangle$ and $\langle \mathrm{PE}' \rangle$ respectively, for the same runs. $\langle \mathrm{KE}' \rangle$

and $\langle \mathrm{PE}' \rangle$ are defined in Fourier space by summing all mode contributions except for the primary wave.

The overall behaviour of $\langle \mathrm{KE} \rangle$ and $\langle \mathrm{PE} \rangle$ consists of a general decrease, because the primary wave is not forced. Three stages can be distinguished in time.

During the first stage, the decay of the kinetic and potential energy of the flow is dominated by molecular dissipation: this is attested by the dotted line plotted in figure 1(*a*), which is the temporal evolution of either energy subjected to molecular effects only. Figure 1(*c*) shows that the perturbation kinetic and potential energy grow exponentially during this stage and remain very close. As we shall see, the perturbation draws energy from the primary wave mostly through resonant interactions. The corresponding loss of energy for the primary wave is, however, not visible in figure 1(*a*) because the perturbation has a very low energy level.

There follows a change in the flow behaviour, characterized by a sudden decrease of the overall flow energy (figure 1*a*) and by the saturation and dissipation of the perturbation energy (figure 1*c*). The wave field starts breaking from this time, which we shall refer to as the breaking time. The breaking process results from the instability of the whole wave field, as will be shown in the final part of the paper. This instability is triggered by the increase in amplitude of the perturbation (and not of the primary wave).

A relaxation regime eventually follows, during which kinetic energy exceeds potential energy for the highest-amplitude runs. Since the domain-averaged kinetic and potential energy are controlled by the energy content of the largest scales, this behaviour may be attributed to the higher transfer rate of potential energy than kinetic energy toward small scales, as we show later in this paper; the two-dimensional geometry of the computations (which prevents kinetic energy from being transferred toward small scales) may also come into play.

In the absence of viscous and diffusive effects, the growth rate of the perturbation from resonant interactions is proportional to the primary wave amplitude A_0 (see equation (8) below), so that the breaking time should be proportional to $1/A_0$, in the limit of small viscosity. This is attested in figure 1(*b*) where $\langle \mathrm{KE} \rangle$ and $\langle \mathrm{PE} \rangle$ are plotted versus time multiplied by Fr_0: the breaking time for the low steepness runs 0, 1 and 2 no longer depends upon the primary wave amplitude with this scaling. The curves match up to the breaking time, but separate from this time on, indicating that a new flow regime commences. Also, in figure 1(*c*) where the same time scaling is used, the perturbation energy grows at the same rate and saturates at the same time for runs 0, 1 and 2. We note from figure 1(*c*) that the perturbation grows at a higher rate for run 3 than for the other runs, consistent with breaking occurring at an earlier time for this run (see figure 1*b*). This implies that, in run 3, the finite amplitude of the primary wave affects the instability process.

In the standing-wave simulations of Bouruet-Aubertot *et al.* (1995), the same evolution of the energy of the overall flow and of the perturbation was found, except that the breaking time scales as $1/A_0^2$ in this case, owing to the difference in initial and boundary conditions.

4. Resonant interaction theory

In this section, we apply resonant interaction theory to the two-dimensional simulations and show that the growth of the perturbation is controlled by a few parametrically resonant triads of comparable growth rates, the values of which are predicted well by the theory.

4.1. *Background*

Resonant interaction theory may be used to investigate the stability of a primary wave whose steepness is much smaller than 1.

Interactions among gravity waves in a stratified fluid occur within triads, because of the quadratic nonlinearity of the equations of motion. At first order in an expansion in the normalized wave amplitude, efficient wave interactions occur if, in addition to the usual spatial resonance condition

$$\boldsymbol{k}_0 + \boldsymbol{k}_1 + \boldsymbol{k}_2 = 0, \tag{6}$$

a temporal resonance condition is also satisfied (Phillips 1977)

$$\omega_0 + \omega_1 + \omega_2 = 0, \tag{7}$$

where $(\boldsymbol{k}_i, \omega_i)_{0 \leqslant i \leqslant 2}$ are the wave vector and frequency of the members of the triad. In this section only, we follow the convention that both negative and positive frequencies are possible, to avoid negative signs in the temporal resonance condition. When a primary wave (associated with index $i = 0$) interacts with two secondary waves of much smaller amplitude, resonant interactions among this triad may lead to instability of the primary wave. As proved by Hasselmann (1967), this occurs when the frequency (in absolute value) of each secondary wave is smaller than the primary wave frequency (in absolute value as well): these are sum interactions $|\omega_1| + |\omega_2| = |\omega_0|$. By contrast, difference interactions $||\omega_1| - |\omega_2|| = |\omega_0|$ are neutrally stable. In principle, triads are coupled with each other, since any member of a triad may also be involved in other triads (an instability process involving coupled triads is discussed in Chow, Henderson & Segur 1996). In the present paper, we only consider one class of triads, those involving the primary wave $(\boldsymbol{k}_0, \omega_0)$, and assume all triads to be isolated from each other. As we shall see, this simplified approach proves to account adequately for the instability of the primary wave in our numerical simulations.

In the following, waves distinct from the primary wave will be referred to as secondary waves, the set of the latter waves forming the perturbation. This is valid in the early stage of the flow development, when the coherence of the primary wave is preserved. Resonantly excited secondary waves will be referred to as resonant waves.

4.2. *Resonant traces and unstable secondary waves*

The resonance conditions (6)–(7) may be solved numerically for a given primary wave $(\boldsymbol{k}_0, \omega_0)$. Following Phillips (1977), the loci of the tip of, say, $\boldsymbol{k}_1$ define the resonant traces. These traces are plotted in figure 2(*a*) for the primary wave $\boldsymbol{k}_0$ considered throughout the paper. The third member of the triad $\boldsymbol{k}_2$ is easily inferred from the spatial resonance condition as indicated in the figure. The branches labelled A, B, D and E and the arcs connecting A and B, and D and E, correspond to sum interactions. In the limit of large wave vector moduli, the branches (and consequently the wave vectors lying along them) have as asymptotes the straight lines whose angle with the horizontal, denoted $\theta_{1/2}$, meets $|\cos\,\theta_{1/2}| = |\cos\,\theta_0|/2$. The corresponding frequencies therefore meet $|\omega_{1/2}| = |\omega_0|/2$, so that the branches are called parametric sub-harmonic instability branches (Phillips 1977). The triads defined by the closed loops labelled C and F correspond to difference interactions and are therefore neutrally stable.

The traces may now be used to identify the secondary waves most unstable to parametric sub-harmonic instability in the numerical simulations: these are the sets of pairs of wavenumbers located at grid points lying on or close to the resonant branches A, B, D and E and whose distance from each other is the primary wave vector. Resonant waves whose energy exceeds 10^{-4} parts of the instantaneous primary

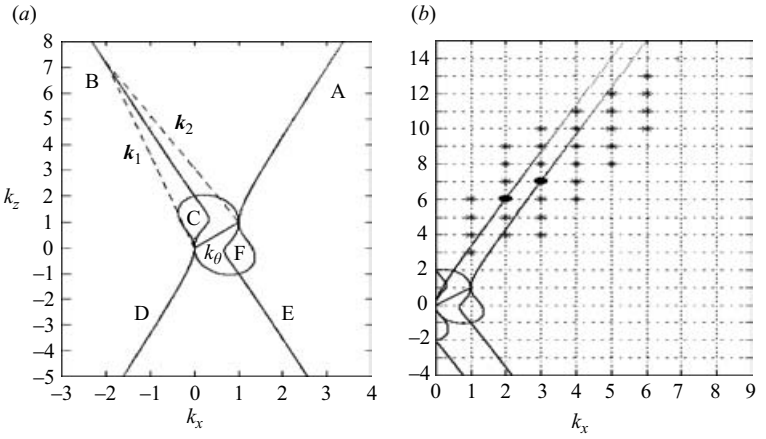

FIGURE 2. (*a*) Theoretical resonant traces for the primary wave $\boldsymbol{k}_0 = (1, 1)$. The traces result from the plot of the tip of wave vector $\boldsymbol{k}_1$, given a wave vector $\boldsymbol{k}_2$ such that the resonance conditions are satisfied. One such resonant triad is drawn using dashed lines for $\boldsymbol{k}_1$ and $\boldsymbol{k}_2$. (*b*) Superposition of the most unstable resonant waves found numerically for run 2 (∗) upon the theoretical resonant traces displayed in (*a*). For illustration, the waves with wave vectors $(2, 6)$ and $(-3, -7)$ (which form triad T_1 with the primary wave) are drawn with a black circle. Resonant traces corresponding to $k_x < 0$ have been reflected through the origin, owing to the Hermitian symmetry of the fields in Fourier space. The numerical grid is also displayed.

wave energy are displayed in figure 2(*b*) for run 2. This threshold test is validated as long as the root mean square (r.m.s.) vorticity of the flow is less than the Brunt–Väisälä frequency (following Bouruet-Aubertot *et al.* 1995), to ensure that resonant interaction theory is assessed well before wave breakdown.

It is apparent that the instability dynamics are controlled by a few resonant triads (as well as by other off-resonant waves). All of these excited waves lie very close to or in the neighbourhood of branches A and D. In figure 2(*b*), the triads $[\boldsymbol{k}_0, \boldsymbol{k}_1, \boldsymbol{k}_2] = [(1, 1), (-2, -4), (1, 3)]$, denoted T_0, $T_1 = [(1, 1), (-3, -7), (2, 6)]$, $T_2 = [(1, 1), (-4, -10), (3, 9)]$ and $T_3 = [(1, 1), (-5, -12), (4, 11)]$ can be identified as being resonantly excited by the instability process (the same result is observed for the other runs, including run 3). Because the discrete nature of the computational grid quantizes the wavenumbers, none of these triads meets the temporal resonance condition (7) exactly. Indeed, the frequency detuning $\omega_0 + \omega_1 + \omega_2$ is equal to -0.056 for triad T_0, with each frequency being of order 1, to -0.019 for T_2 and T_3, and to -0.0030 only for triad T_1. Hence, the latter triad meets the temporal resonance relation most closely. Strict temporal resonance is not required for the existence of resonant triads as shown by McEwan & Plumb (1977) and discussed by Craik (1985), but instead it need only be satisfied within a precision of the order of the steepness. Note that the quantization by the grid size becomes insignificant for high wavenumbers. In a viscous fluid, the high-wavenumber waves are actually damped by viscous and diffusive effects so that, in a numerical simulation, the most unstable resonant waves are selected by viscous and diffusive effects and by the grid size.

The triad T_1 was also found to be the most resonant one by Bouruet-Aubertot *et al.* (1995) in the standing primary wave case, probably because the initial condition of their computations is a superposition of four counter-propagating progressive waves with wave vector $(\pm 1, \pm 1)$. They also observed many temporally non-resonant triads

and isolated secondary wave modes, which were interpreted as being entrained by nonlinear interactions with the resonant triads.

4.3. *Growth rates of the resonant waves*

4.3.1. *Growth rates predicted by resonant interaction theory*

The growth rates of resonant waves are easily predicted by the resonant interaction theory at first order, if it is assumed that the primary wave amplitude remains constant during the growth of the resonant waves and that the amplitudes of these waves are simply damped by molecular effects (McEwan & Plumb 1977). As a result, the resonant waves $(\boldsymbol{k}_1, \omega_1)$ and $(\boldsymbol{k}_2, \omega_2)$ may amplify exponentially in time, with growth rate

$$\lambda = -\tfrac{1}{2}(T_1 + T_2) + \left[\tfrac{1}{4}(T_1 - T_2)^2 + S_1 S_2 \frac{A_0^2}{4}\right]^{1/2}, \tag{8}$$

provided λ is real and positive. $T_i = \frac{1}{2}\nu(1 + 1/Pr)\kappa_i^2$ is the linear damping factor of wave i in the triad, $i = 1$ or 2 and S_i is the interaction coefficient:

$$S_i = \frac{1}{2\kappa_i^2 \omega_i}\left[\omega_i\left(\kappa_p^2 - \kappa_q^2\right) + N^2 k_i\left(\frac{k_p}{\omega_p} - \frac{k_q}{\omega_q}\right)\right](m_q k_p - m_p k_q), \tag{9}$$

where p and q assume different integer values selected from 0, 1 or 2. Equation (8) shows that unstable solutions are possible provided that (i) $S_1 S_2 > 0$ and (ii) the constant amplitude A_0 of the primary wave exceeds the threshold value given by: $A_{th} = 2\sqrt{T_1 T_2 / S_1 S_2}$. The first condition may be shown to be equivalent to Hasselmann's (1967) criterion discussed in § 4.1. The second condition ensures that growth due to nonlinear interaction is larger than decay due to molecular effects.

For very large wavenumbers of the resonant waves, resonance occurs through parametric instability and, in the inviscid case, their growth rate tends toward the asymptotic expression

$$\lambda_\infty = \tfrac{1}{8} A_0 \kappa_0^2 \cos^2\theta_0 [\tan(\theta_1) - \tan(\theta_0)][3 - \sin(\theta_1 - \theta_0)\tan\theta_1], \tag{10}$$

with θ_1 such that $\cos\theta_1 = (\cos\theta_0)/2$. Equation (10) matches an equivalent expression proposed by Sonmor & Klaassen (1997) (but note that κ_0 is set to 1 in their analysis and therefore, does not appear in their expression; also the amplitude A in their expression is twice ours: $A = 2A_0$).

The growth rates associated with the four branches A, B, D and E are plotted in figure 3 both for the inviscid and viscous cases, for run 2 (that is, the values of A_0 and ν in (8) are those of run 2). The value of the threshold amplitude for this run is $A_{th} = 3.68 \times 10^{-2}$, which is lower than A_0 (= 0.256) so that secondary waves can be parametrically excited. The value of λ_∞ is equal to 0.10 for run 2. Figure 3(*a*) shows that, in the inviscid limit, this value is approached to better than 1 % when $\kappa_1 \geqslant 7$. However, viscous and diffusive effects have a strong influence and select rather large-scale resonant waves, as the growth rate is now maximum for $\kappa_1 \simeq 5$. For $\kappa_1 \geqslant 2$, triads lying along branches B and E have smaller growth rates than triads lying along branches A and D. This is consistent with the results found in the threshold test discussed above, where no excitation of waves lying along branches B and E was found.

4.3.2. *Growth rates computed from DNS*

In this section, we compare the growth rate of resonant waves selected by the numerical threshold test (discussed in § 4.1) to the theoretical prediction, (8). Results

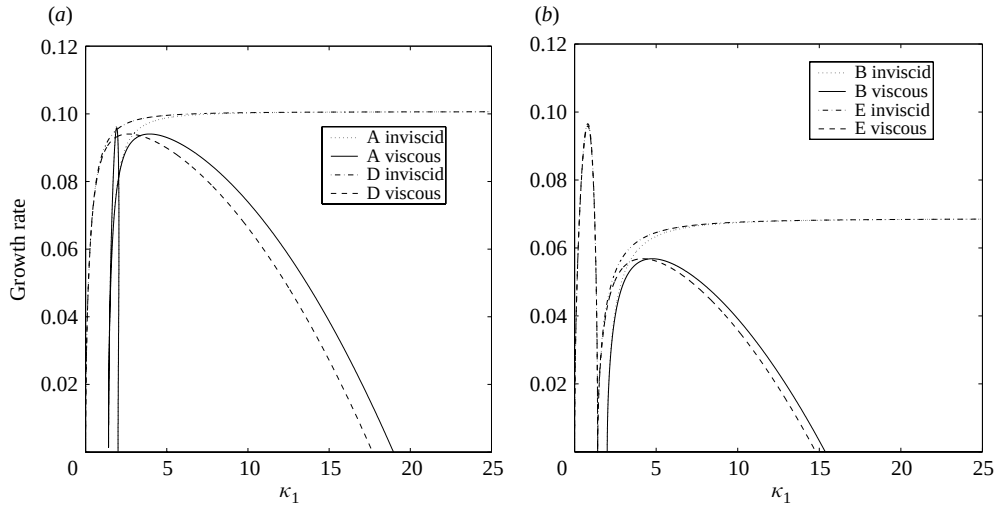

FIGURE 3. Theoretical predictions of the inviscid and viscous growth rates (defined by (8)) for the parameters of run 2, as a function of the modulus of wavenumber $\boldsymbol{k}_1$ (denoted κ_1), along the branches displayed in figure 2(*a*). The growth rates are normalized by the Brunt–Väisälä frequency.

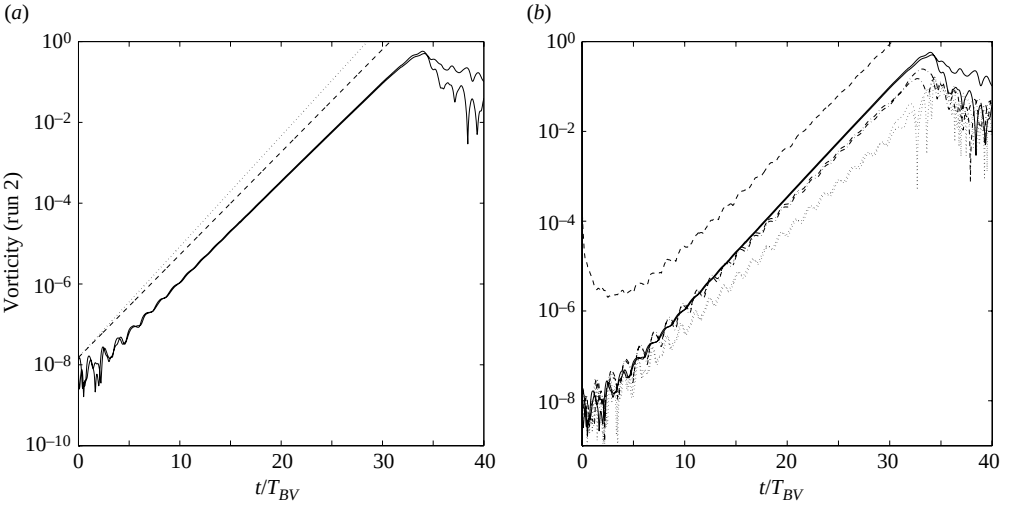

FIGURE 4. (*a*) Absolute value of the vorticity of resonant waves (2, 6) and (−3, −7) as obtained from DNS run 2 (full lines) compared with theoretical growth rate (8) from resonant interaction theory in the inviscid limit (dotted line) and when molecular effects are taken into account (dashed line); (*b*) DNS results only: absolute value of the vorticity of resonant waves (2, 6) and (−3, −7) (full lines), (3, 9) and (−4, −10) (dash-dotted lines), (4, 11) and (−5, −12) (dotted lines) and maximum absolute value of the perturbation vorticity (dashed line).

for triad T_1 in run 2 are displayed in figure 4(*a*); the vorticity (in absolute value) of the resonant waves in this triad is plotted versus time, using a log–lin scale. The vorticity of each wave grows exponentially at the same rate and, at least during 15 Brunt–Väisälä periods or so, this rate matches the theoretical viscous growth rate. We performed the same comparison between numerical and theoretical growth rates

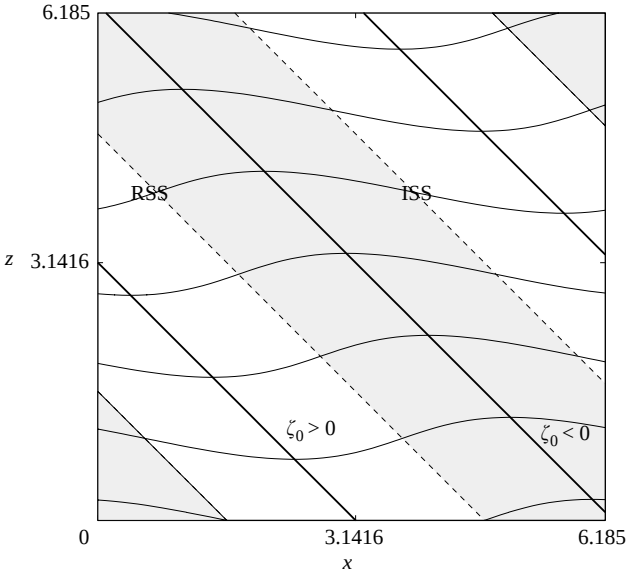

FIGURE 5. Detailed structure of the primary internal gravity wave $\boldsymbol{k}_0 = (1, 1)$ for run 2. Constant density lines and constant phase lines of the wave are displayed. Areas with increased or reduced static stability are denoted by ISS or RSS, respectively, and delimited by thick phase lines. Shaded areas are associated with negative primary wave vorticity $\zeta_0 < 0$ and light areas with positive vorticity $\zeta_0 > 0$.

for triads T_2 and T_3 in the same run (not shown). A stronger difference between the viscous and inviscid growth rates is observed because the wavenumber of each resonant wave is higher than for triad T_1. As for the latter triad, the numerical growth rate matches well the theoretical viscous growth rate during the early stage of the instability development.

The numerical growth rates of the resonant waves in these three triads are superimposed in figure 4(*b*). All three rates are comparable, with the triads T_1 and T_2 growing at the same rate during 15 T_{BV} or so. The maximum value over the numerical domain of the vorticity of the perturbation is also displayed in the figure. Its growth rate is very close to that of the resonant triads. This implies that the resonant process controls the instability of the primary wave, through the parametric excitation of a few waves with nearly identical growth rates, which entrain the non-resonant waves of the flow. This is an important result for our analysis of the parametric instability.

5. The structure of the instability in physical space

In this section, we derive a simple kinematic model of the instability in physical space based upon a single resonant triad, in which the secondary waves are parametrically forced by the primary wave. We show in particular that the model reproduces very well the vorticity field of the perturbation computed from DNS.

5.1. *The spatial structure of a linear internal gravity wave*

Figure 5 shows the detailed structure of the primary internal gravity wave we consider throughout the paper, plotted in a $(2\pi)^2$ periodic geometry for run 2. The phase lines propagate along the direction defined by $\boldsymbol{k}_0$, i.e. towards the upper right-hand corner of the domain. At any given time, the domain may be subdivided into areas defined

by the internal wave properties. Thus, we distinguish zones according to the sign of the primary wave vorticity ζ_0, shaded areas corresponding to $\zeta_0 < 0$ and light areas to $\zeta_0 > 0$. In §6.3, these areas will also be referred to as an N region and a P region, respectively. Similarly, we distinguish zones according to the sign of the vertical density gradient of the primary wave. Positive values of this gradient reduce the static stability set by the background stratification and negative values increase that stability; the former zone will be denoted by RSS and the latter by ISS. Zones defined by the sign of the vorticity ζ_0 overlap evenly with zones defined by the sign of the vertical density gradient, because these two fields are out of phase by $\pi/2$. All zones considered translate in time at the phase speed of the primary wave.

5.2. *A simple model for the kinematics of the resonant secondary waves*

The resonant interaction theory applied in the last section has led to the conclusion that the primary wave instability is governed by a few resonant triads, selected among all possible resonant triads by the molecular properties of the fluid (viscosity and diffusivity) and by the grid size. The secondary waves involved in these triads have approximately the same amplitude and grow at about the same rate, which agrees well with the theoretical growth rate. A basic assumption of the theory is that these triads do not interact with each other. The triads may thus be assumed to grow independently, at least during the early stage of the wave-field evolution. Therefore, the energy exchange processes with the primary wave may be addressed by considering one triad only. We shall choose triad T_1. We adopt from now on the convention that frequencies are positive. The temporal resonance condition is thus expressed as $\omega_1 + \omega_2 = \omega_0$ and the associated spatial resonance condition as $\boldsymbol{k}_1 + \boldsymbol{k}_2 = \boldsymbol{k}_0$. In the following, $\boldsymbol{k}_0 = (1, 1)$, $\boldsymbol{k}_1 = (3, 7)$ and $\boldsymbol{k}_2 = (-2, -6)$ (so that $\omega_1 = N\cos(\theta_1)$ and $\omega_2 = -N\cos(\theta_2)$).

Let A' be the amplitude of the secondary resonant waves in this triad. As long as their steepness is much smaller than 1, insight into the kinematics of the instability can be gained by simply superimposing these two waves. The resulting streamfunction is, using the polarization relations, (4):

$$A'[\sin(\boldsymbol{k}_1 \cdot \boldsymbol{x} - \omega_1 t) + \sin(\boldsymbol{k}_2 \cdot \boldsymbol{x} - \omega_2 t + \phi')], \tag{11}$$

while the resulting density field is:

$$A' N \kappa_1 [\sin(\boldsymbol{k}_1 \cdot \boldsymbol{x} - \omega_1 t) - \sin(\boldsymbol{k}_2 \cdot \boldsymbol{x} - \omega_2 t + \phi')], \tag{12}$$

where ϕ' is the phase difference between the two waves. A good approximation for these fields can be obtained by assuming that the resonant waves are of small scale relative to the primary wave, implying that (i) $\kappa_0 \ll \kappa_1, \kappa_2$; $\boldsymbol{k}_1 \simeq -\boldsymbol{k}_2$ so that $\boldsymbol{k}_1 - \boldsymbol{k}_2 \simeq 2\boldsymbol{k}_1$ but $\boldsymbol{k}_1 + \boldsymbol{k}_2 = \boldsymbol{k}_0$; (ii) temporal resonance is nearly satisfied: $\omega_1 \simeq \omega_2 \simeq \omega_0/2$, with $\delta\omega = \omega_1 - \omega_2 \ll \omega_1, \omega_2$. $\delta\omega$ is the frequency mismatch between the two resonant waves. With these assumptions, the approximate expressions for the resulting streamfunction (11) and density fields (12), which we denote as $\tilde{\psi}$ and $\tilde{\sigma}$, are:

$$\tilde{\psi}(x, z, t) = 2A' \sin\left(\tfrac{1}{2}\boldsymbol{k}_0 \cdot \boldsymbol{x} - \tfrac{1}{2}\omega_0 t + \tfrac{1}{2}\phi'\right) \cos\left(\boldsymbol{k}_1 \cdot \boldsymbol{x} - \tfrac{1}{2}\delta\omega\, t - \tfrac{1}{2}\phi'\right), \tag{13}$$

$$\tilde{\sigma}(x, z, t) = 2A' N \kappa_1 \cos\left(\tfrac{1}{2}\boldsymbol{k}_0 \cdot \boldsymbol{x} - \tfrac{1}{2}\omega_0 t + \tfrac{1}{2}\phi'\right) \sin\left(\boldsymbol{k}_1 \cdot \boldsymbol{x} - \tfrac{1}{2}\delta\omega\, t - \tfrac{1}{2}\phi'\right). \tag{14}$$

The interpretation of (13) and (14) is straightforward: each scalar field represents a wave with wavevector $\boldsymbol{k}_1$ propagating with the phase velocity $\delta\omega/(2\kappa_1)$, whose amplitude is modulated by a sinusoidal envelope of wavelength $4\pi/\kappa_0$ that propagates at the phase speed of the primary wave. Since the side of the numerical domain is 2π only, the modulation will consist of half a sinusoidal envelope, of width $2\pi/\kappa_0$.

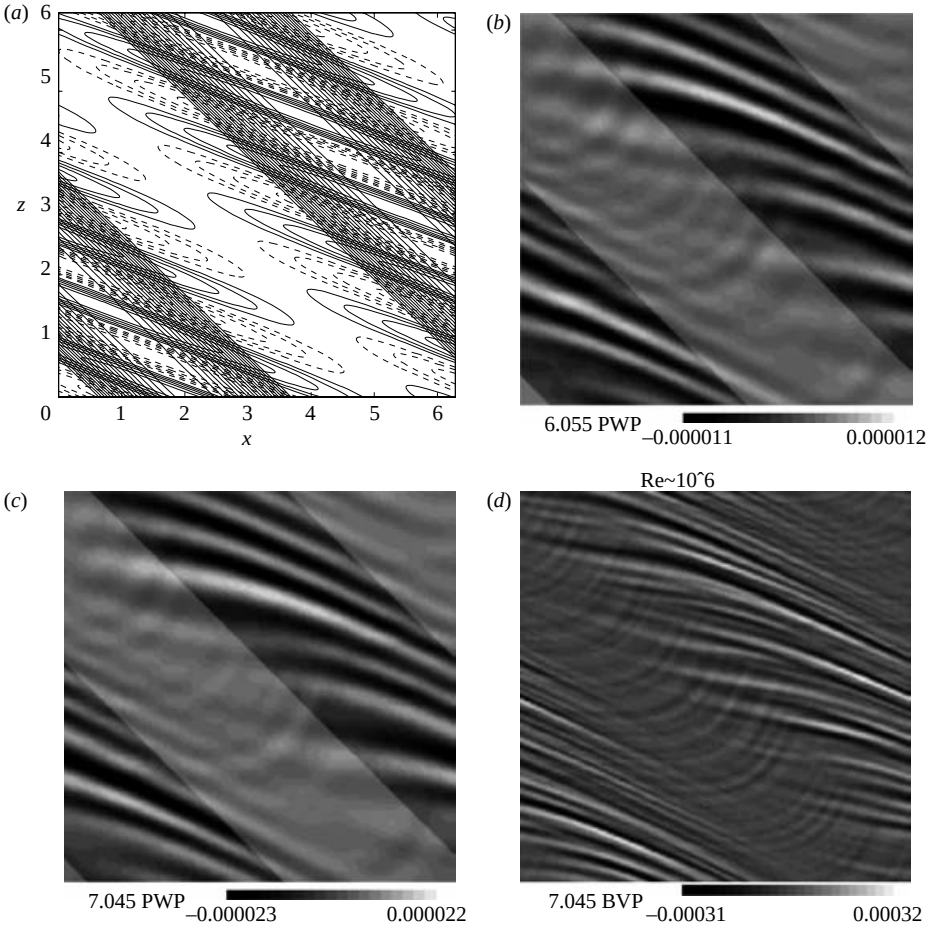

FIGURE 6. (*a*) Contours of the vorticity field, (15), for the resonant secondary waves of triad T_1, using the triad model (negative values are represented by dotted lines). Negative values of the primary wave vorticity field, (16), manifested as dark tilted bands, are superimposed. (*b*, *c*) Contours of the perturbation vorticity field computed from the DNS run 2 at two instants separated by one primary wave period (PWP). Regions of negative and positive sign of the primary wave vorticity ζ_0 are superposed (dark regions: $\zeta_0 < 0$, light regions: $\zeta_0 > 0$). (*d*) Perturbation vorticity field for a run identical to run 2 except that the viscosity is smaller by two orders of magnitude (the primary wave vorticity is not shown here).

The width of the envelope is much greater than the typical wavelength ($2\pi/\kappa_1$) of the oscillations modulated by the envelope. Consequently, any spatial derivative of $\tilde{\psi}$ (or $\tilde{\sigma}$) is approximated well by differentiating with respect to the latter oscillations only. In this approximation, the vorticity of the resonant waves $\tilde{\zeta} = \nabla^2\tilde{\psi}$ is expressed by

$$\tilde{\zeta}(x, z, t) = -2\kappa_1^2 A' \sin\left(\tfrac{1}{2}\boldsymbol{k}_0 \cdot \boldsymbol{x} - \tfrac{1}{2}\omega_0 t + \tfrac{1}{2}\phi'\right) \cos\left(\boldsymbol{k}_1 \cdot \boldsymbol{x} - \tfrac{1}{2}\delta\omega\, t - \tfrac{1}{2}\phi'\right). \qquad (15)$$

This field is visualized for triad T_1 at a given time in figure 6(*a*). The spatial structure of $\tilde{\zeta}$ within the envelope consists of alternating crests and troughs whose normal directed along $\boldsymbol{k}_1$ makes an angle θ_1 with the horizontal such that $\cos\theta_1 \simeq (\cos\theta_0)/2$. The latter feature simply reflects the parametric resonance excitation of the secondary waves.

Expressions (13) and (14) also show that the phase within the envelope propagates at a much smaller speed than the envelope does. Indeed, the two relevant speeds are in the ratio $[\omega_0/\kappa_0]/[\delta\omega/(2\kappa_1)] \simeq 100$ for triad T_1. The oscillation within the envelope can thus be considered as stationary with respect to the fluid domain. The phase lines would be exactly stationary, were the temporal resonance condition exactly satisfied. This peculiar property is related to the quasi-opposite propagation of the resonant waves (i.e. $\boldsymbol{k}_1 \simeq -\boldsymbol{k}_2$). Neglecting the phase propagation within the envelope, any scalar field of the resonant waves ($\tilde{\psi}$, $\tilde{\sigma}$ or $\tilde{\zeta}$) therefore has a temporal period of two primary wave periods. We shall see that this structure of the resonant waves is the key to optimizing the energy exchange with the primary wave.

5.3. *Spatial structure of the instability in the numerical simulations*

Contours of the perturbation vorticity field are displayed in figures 6(*b*) and 6(*c*) for run 2 at two instants separated by one period of the primary wave. Regions of positive and negative sign of the primary wave vorticity field ζ_0 are superimposed in order to investigate the phase relationship between the two fields.

Despite the fact that several resonant (and non-resonant) triads grow simultaneously, the structure of the perturbation vorticity field matches the predictions by the simple triad model: the field displays a modulation of width $2\pi/\kappa_0$, the vorticity changes sign between figures 6(*b*) and 6(*c*) at any given point and the phase oscillations within the envelope are manifested as alternating crests and troughs whose normal makes an angle close to $\cos^{-1}(0.5\ \cos\theta_0)$ with the horizontal. The adequacy of the triad model to predict this pattern confirms the dominant role of a few independent resonant triads in the primary wave instability. The length scale of the vorticity bands within the envelope, δ say, is set by the typical wavelength of the resonant waves, $\delta \simeq \pi/\kappa_1$. This is confirmed in figure 6(*d*), which displays the vorticity field of the perturbation for a computation identical to run 2 except that it uses a viscosity smaller by two orders of magnitude; wave vectors with a larger modulus are selected by the smaller viscosity which sets thinner vorticity bands. This thickness is therefore controlled by the wave vector of the primary wave, by molecular effects and, for large enough viscosity, by the grid resolution. The growth of the perturbation is attested by the fact that the perturbation vorticity increases by a factor 2 (from 1.1×10^{-5} to 2.2×10^{-5}) between figures 6(*b*) and 6(*c*).

Compared to figure 6(*a*), figure 6(*b*) still displays an important difference, when the perturbation vorticity field alone is considered. This difference is best put forward by a clockwise rotation of the (x, z)-coordinate system through $\pi/2 - \theta_1$. In the resulting (x', z')-coordinate system the perturbation vorticity field may be viewed as a horizontally periodic wave packet confined along the vertical z'-direction. Figure 6(*b*) shows that the tail of the vorticity bands is tilted toward the z'-axis and thickens while tilting. Such effects are also observed by Sutherland (2001) in studying finite-amplitude horizontally periodic, vertically compact wave packets (see figure 4 of his paper). According to Sutherland, nonlinear effects resulting from the interaction of the wave field with its induced mean flow may trigger a process of self-acceleration, which accounts for the observed modifications in the wave packet structure. In the present case, the secondary wave amplitude is too small to yield any significant induced mean flow, but the large-scale flow associated with the primary wave may act as such a mean flow. Hence, the observed effects could be a manifestation of the finite amplitude of the primary wave.

A striking feature of figure 6(*b*) is that the perturbation vorticity $\tilde{\zeta}$ reaches extremal values when the primary wave vorticity $\zeta_0 < 0$ is negative. This feature is inherent to

the parametric forcing mechanism as will be seen in the next section. The envelope of $\tilde{\zeta}$ and the $\zeta_0 < 0$ zone should then remain in phase during the instability growth since (using the triad model) they propagate at the same speed. The phase of the primary wave relative to the envelope of $\tilde{\zeta}$ can easily be inferred from this model. Writing that the envelope $\sin(\boldsymbol{k}_0 \cdot \boldsymbol{x}/2 - \omega_0 t/2 + \phi'/2)$ (see relation (15)) reaches an extremal value when $\zeta_0 = -A\kappa_0^2 \sin(\boldsymbol{k}_0 \cdot \boldsymbol{x} - \omega_0 t + \phi)$ is minimum yields $\phi = \phi' - \pi/2$ mod. 2π. This means that the forcing of the resonant waves results from an adjustment of the phase within the triad such that

$$\zeta_0(x, z, t) = A\kappa_0^2 \cos(\boldsymbol{k}_0 \cdot \boldsymbol{x} - \omega_0 t + \phi'), \tag{16}$$

when (15) is used for $\tilde{\zeta}$. With the present definition of ψ_0 (see (4)), $\phi = 0$ so that $\phi' = \pi/2$, but we shall keep the phase difference ϕ' in the remainder of the paper for more generality. Contours of negative values of ζ_0 given by (16) are superimposed upon contours of $\tilde{\zeta}$ in figure 6(*a*). The former contours lie in the region of extremal values of the envelope, by construction, and closely model the spatial structure displayed in figure 6(*b*).

6. Energetics of the instability

In this section, we analyse the energy exchange process between the primary wave and the parametrically forced resonant waves. Analytical expressions for the energy exchange terms are derived from the kinematic model, which are compared for triad T_1 to the DNS results, for runs 0, 2 and 3.

6.1. *Linearized equations for the perturbation energy*

The instability mechanism through which the perturbation grows is best analysed using energy budgets in the classical rotated frame of reference (e.g. Mied 1976): $X = x \sin\theta_0 - z\cos\theta_0$, $Z = x\cos\theta_0 + z\sin\theta_0$. This frame of reference provides a simpler expression for the velocity field (U_0, W_0) and for the density field Σ_0 of the primary wave: $[U_0, W_0, \Sigma_0] = [A\kappa_0 \sin\Phi_0, 0, -A\,N\kappa_0 \cos\Phi_0]$, with $\Phi_0 = k_0 x + m_0 z - \omega_0 t + \phi' = \kappa_0 Z - \omega_0 t + \phi'$.

We perform a decomposition of the flow fields into primary wave components and perturbation components following

$$\boldsymbol{U} = \boldsymbol{U}_0 + \boldsymbol{U}' \quad \rho' = \Sigma_0 + \sigma' \quad p = P_0 + P', \tag{17}$$

where $\boldsymbol{U}$ refers to the total velocity field in the rotated reference frame. Linearization of the Boussinesq equations in this rotated reference frame yields the following equations for the energy of the perturbation, ignoring molecular effects (e.g. Lombard & Riley 1996*a*; Sonmor & Klaassen 1997):

$$\left(\frac{\mathrm{D}}{\mathrm{D}t}\right)_0 \tfrac{1}{2}(U'^2 + W'^2) = -\nabla(\boldsymbol{U}' \cdot P') - \sigma'(-U'\cos\theta_0 + W'\sin\theta_0) - U'W'\zeta_0, \tag{18}$$

$$\left(\frac{\mathrm{D}}{\mathrm{D}t}\right)_0 \frac{1}{2}\frac{\sigma'^2}{N^2} = \sigma'(-U'\cos\theta_0 + W'\sin\theta_0) - \frac{1}{N^2}\sigma' W' \frac{\mathrm{d}\Sigma_0}{\mathrm{d}Z}. \tag{19}$$

The expression $(\mathrm{D}/\mathrm{D}t)_0 = \partial/\partial t + U_0 \partial/\partial X$ is the material derivative following the primary wave and ∇ now denotes the gradient with respect to the rotated coordinate system.

The right-hand side of equation (18) shows that the rate of change of the perturbation kinetic energy per unit mass $\mathrm{KE}' = (U'^2 + W'^2)/2$ is contributed to by three

terms, (i) the net rate of working by pressure forces on the unit mass, (ii) minus the perturbation buoyancy flux, denoted as $-\mathrm{BF}'$ in what follows, and (iii) the kinetic energy transfer rate between the primary wave and the perturbation. BF' has the well-known expression $\sigma' w'$, since w' becomes $(-U' \cos\theta_0 + W' \sin\theta_0)$ under the coordinate system transformation. Term (iii) involves the shear of the primary wave, since $\zeta_0 = \mathrm{d}U_0/\mathrm{d}Z$, and will be referred to as the perturbation kinetic energy production term, or KEP for short. Similarly, equation (19) shows that the rate of change of the perturbation potential energy per unit mass $\mathrm{PE}' = 1/2(\sigma'^2/N^2)$ is driven by the buoyancy flux BF' and by a perturbation potential energy production term; the latter term is denoted by PEP and involves the vertical density gradient of the primary wave $\mathrm{d}\Sigma_0/\mathrm{d}Z$ (Lombard & Riley 1996*a*). Note that both energy exchange terms KEP and PEP can be of either sign.

6.2. *Predictions of the kinematic triad model*

To obtain an insight into the parametric forcing process, it is useful to obtain explicit expressions of these energy exchange terms. Approximate expressions may be obtained from the kinematic triad model introduced in the previous section. In the following, any quantity derived from the model (therefore involving the two secondary waves resonantly interacting with the primary wave) will be denoted with a tilde.

The velocity field of the resonant waves can be computed from (13) for the resulting streamfunction $\tilde{\psi}$. As for the computation of the resulting vorticity, (15), spatial differentiation is performed with respect to spatial oscillations within the envelope, the change in the slowly varying envelope being neglected. This operation yields (in the rotated reference frame)

$$\widetilde{U} = -2A'\kappa_1 \cos(\theta_1 - \theta_0) \sin\left(\tfrac{1}{2}\Phi_0\right) \sin\Phi_1, \quad \widetilde{W} = -2A'\kappa_1 \sin(\theta_1 - \theta_0) \sin\left(\tfrac{1}{2}\Phi_0\right) \sin\Phi_1, \tag{20}$$

where $\Phi_1 = \boldsymbol{k}_1 \cdot \boldsymbol{x} - (\delta\omega/2)t - \phi'/2$. Il follows that

$$\frac{\widetilde{U}\widetilde{W}}{(A'\kappa_1)^2} = 2 \sin[2(\theta_1 - \theta_0)] \sin^2\left(\tfrac{1}{2}\Phi_0\right) \sin^2\Phi_1. \tag{21}$$

$(A'\kappa_1)^2$ is the total energy of the resonant waves. The expression for the energy exchange terms $\widetilde{\mathrm{KEP}} = -\tilde{U}\tilde{W}\zeta_0$ and $\widetilde{\mathrm{PEP}} = -(1/N^2)\tilde{\sigma}\widetilde{W}(\mathrm{d}\Sigma_0/\mathrm{d}Z)$ are readily obtained:

$$\frac{\widetilde{\mathrm{KEP}}}{(A'\kappa_1)^2} = -2A_0\kappa_0^2 \sin[2(\theta_1 - \theta_0)] \sin^2\left(\tfrac{1}{2}\Phi_0\right) \cos\Phi_0 \sin^2\Phi_1, \tag{22}$$

$$\frac{\widetilde{\mathrm{PEP}}}{(A'\kappa_1)^2} = 2A_0\kappa_0^2 \sin(\theta_1 - \theta_0) \sin^2\Phi_0 \sin^2\Phi_1. \tag{23}$$

Since $0 \leqslant 2(\theta_1 - \theta_0) \leqslant \pi/2$, $\sin[2(\theta_1 - \theta_0)] \geqslant 0$. Therefore, (i) $\tilde{U}\tilde{W} \geqslant 0$, (ii) the sign of $\widetilde{\mathrm{KEP}}$ is that of $-\cos\Phi_0$, that is of $-\zeta_0$, and (iii) $\widetilde{\mathrm{PEP}} \geqslant 0$. The expression of all the terms related to the energetics of the resonant waves are given in table 2.

The mechanisms of amplification through parametric instability are studied below, but we think it useful to summarize the main ideas now. For simplicity, let us consider the energy exchange processes at one location in the fluid domain. The above remarks about the sign of $\widetilde{\mathrm{KEP}}$ imply that resonant waves extract kinetic energy from the primary wave when ζ_0 is negative at that location. This occurs during half a primary wave period. During the other half period, ζ_0 becomes positive at that location so that

Definition of Q	Prediction of Q by the triad model
ζ_0	$A_0\kappa_0^2\cos\Phi_0$
$\dfrac{\mathrm{d}\Sigma_0}{\mathrm{d}Z}$	$A_0\kappa_0^2 N\sin\Phi_0$
$\widetilde{\mathrm{U}}$	$-2A'\kappa_1\cos(\theta_1-\theta_0)\sin(\frac{1}{2}\Phi_0)\sin\Phi_1$
$\widetilde{\mathrm{W}}$	$-2A'\kappa_1\sin(\theta_1-\theta_0)\sin(\frac{1}{2}\Phi_0)\sin\Phi_1$
$\widetilde{\sigma}$	$2A'N\kappa_1\cos(\frac{1}{2}\Phi_0)\sin\Phi_1$
$\widetilde{\mathrm{KE}}=\frac{1}{2}(\widetilde{U}^2+\widetilde{W}^2)$	$2\sin^2(\frac{1}{2}\Phi_0)\sin^2\Phi_1$
$\widetilde{\mathrm{PE}}=\frac{1}{2}\dfrac{\widetilde{\sigma}^2}{N^2}$	$2\cos^2(\frac{1}{2}\Phi_0)\sin^2\Phi_1$
$\widetilde{\mathrm{BF}}=\widetilde{\sigma}\widetilde{w}$	$\omega_0\sin\Phi_0\sin^2\Phi_1$
$\widetilde{\mathrm{KEP}}=-\widetilde{U}\widetilde{W}\zeta_0$	$-2A_0\kappa_0^2\sin[2(\theta_1-\theta_0)]\sin^2(\frac{1}{2}\Phi_0)\cos\Phi_0\sin^2\Phi_1$
$\widetilde{\mathrm{PEP}}=\dfrac{-\widetilde{\sigma}\widetilde{W}}{N^2}\dfrac{\mathrm{d}\Sigma_0}{\mathrm{d}Z}$	$2A_0\kappa_0^2\sin(\theta_1-\theta_0)\sin^2\Phi_0\sin^2\Phi_1$

TABLE 2. Kinematic triad model. Predictions are expressed as a function of A_0 and A' (primary and resonant wave streamfunction amplitude), θ_0 and θ_1 (angle with the horizontal of the primary wave and resonant waves, respectively), N (Brunt–Väisälä frequency), κ_0 and κ_1 (primary and resonant wave vector modulus), and of the phases of the primary and resonant waves Φ_0 and Φ_1, respectively. The predictions of the last five quantities are normalized by $(\kappa_1 A')^2$ (total energy of the resonant waves).

$\widetilde{\mathrm{KEP}}$ changes sign and becomes positive. The point is that the loss of kinetic energy from the resonant waves will be minimized during this half-period if the latter energy is (reversibly) stored into potential energy; indeed, the value of $\tilde{U}\tilde{W}$ will be minimum during this half-period (but not exactly zero as we shall see). Regarding the resonant wave potential energy, the positive sign of $\widetilde{\mathrm{PEP}}$ implies that these waves extract potential energy from the primary wave whether the local stability is increased by the primary wave ($\mathrm{d}\Sigma_0/\mathrm{d}Z<0$) or decreased ($\mathrm{d}\Sigma_0/\mathrm{d}Z>0$). These remarks imply that an optimum scenario for energy exchange between the primary and resonant waves occurs when the energy of the resonant waves oscillates with the same frequency as the vorticity of the primary wave anywhere in the fluid domain. Or the resonant wave energy is phase-locked with the primary wave vorticity, meaning that the resonant wave frequency should be $\omega_0/2$ and its wavelength $2(2\pi/\kappa_0)$. These remarks explain in particular why the extremal values of the vorticity perturbation coincide in figure 6 with the region where $\zeta_0<0$: this is the location where the perturbation kinetic energy is forced.

These energy transfer mechanisms are illustrated in figure 7. Quantities related to the energetics of the resonant waves are plotted as a function of time, at a given position in the fluid domain. Note that all these quantities are normalized by the total energy of the resonant waves $(\kappa_1 A')^2$ but, for simplicity, we shall keep the same notation to refer to the normalized quantities.

For the resonant triad T_1, the frequency mismatch $\delta\omega=\omega_1-\omega_2$ is not small with respect to ω_0 so that the temporal evolution of the envelope is strongly modulated. For a clear illustration of the exchange process, we ignore this frequency mismatch in the following. From a physical point of view, this amounts to considering a low-viscosity fluid, for which resonant waves of high wavenumber (thus having $\delta\omega\ll 1$) would be

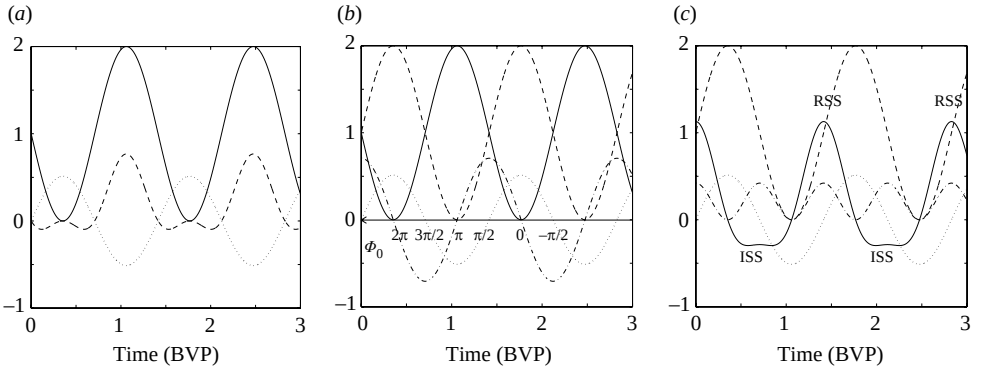

FIGURE 7. Prediction by the kinematic triad model, for resonant waves with large enough wavenumbers so that $|\omega_1 - \omega_2| \ll \omega_0$. Results are shown for a primary wave amplitude equal to $A_0 = 0.256$. All quantities, normalized by the total energy of the resonant waves, are plotted over three Brunt–Väisälä periods at a fixed location in the fluid domain ($x = \pi/4, z = \pi/4$). (*a*) $\widetilde{\mathrm{KE}}$ (full line), $\widetilde{\mathrm{KEP}}$ (dashed line) and ζ_0 (dotted line); (*b*) $\widetilde{\mathrm{KE}}$ (full line), $\widetilde{\mathrm{PE}}$ (dashed line), $\widetilde{\mathrm{BF}}$ (dash-dotted line) and ζ_0 (dotted line); the abscissa is also expressed in term of the primary wave phase Φ_0; (*c*) $\widetilde{\mathrm{PE}}$ (dashed line), $\widetilde{\mathrm{PEP}}$ (dash-dotted line), $\widetilde{\mathrm{PEP}} + \widetilde{\mathrm{BF}}$ (full line) and ζ_0 (dotted line). The RSS (reduced static stability) and ISS (increased static stability) regions are indicated. ζ_0 is the primary wave vorticity and all other quantities have been defined in §§6.1 and 6.2.

selected. This choice also reflects the fact that the energy transfer mechanisms are controlled by the primary wave.

The quantities $\widetilde{\mathrm{KE}}$, $\widetilde{\mathrm{KEP}}$ and ζ_0 are displayed in figure 7(*a*). The transfer of kinetic energy from the primary wave $\widetilde{\mathrm{KEP}}$ is maximum when ζ_0 is minimum, as expected from the expression of $\widetilde{\mathrm{KEP}}$ and from the discussion above. When ζ_0 passes through zero and becomes positive, the forcing term $\widetilde{\mathrm{KEP}}$ becomes slightly negative, which means that the resonant waves still return to the primary wave a small part of the acquired kinetic energy. However, $\widetilde{\mathrm{KEP}}$ vanishes when ζ_0 is maximum, implying that all of the resonant wave energy is under potential form at that time. The latter point is confirmed in figure 7(*b*), where $\widetilde{\mathrm{KE}}$, $\widetilde{\mathrm{PE}}$, $\widetilde{\mathrm{BF}}$ and ζ_0 are displayed as a function of time at the same fixed location relative to the fluid domain.

It follows that the buoyancy flux $\widetilde{\mathrm{BF}}$ should change sign during the half period where ζ_0 has a constant sign. Hence, $\widetilde{\mathrm{BF}}$ should be out-of-phase by $\pi/2$ with ζ_0. Figure 7(*b*) shows that this is the case.

Quantities related to resonant wave potential energy, namely $\widetilde{\mathrm{PE}}$, $\widetilde{\mathrm{PEP}}$ and $\widetilde{\mathrm{PEP}} + \widetilde{\mathrm{BF}}$ are plotted along with ζ_0 in figure 7(*c*) as a function of time. The forcing term PEP remains positive at all times and is maximum where ζ_0 vanishes, which occurs at locations in an RSS or ISS region. At these locations $\widetilde{\mathrm{KE}} = \widetilde{\mathrm{PE}}$, that is, $\widetilde{\mathrm{PE}}$ is only half its maximum value. This accounts for the asymmetry of the forcing of the resonant wave energy by the primary wave: during a primary wave period, $\widetilde{\mathrm{KE}}$ is forced once by the primary wave (at $\Phi_0 = \pi$ mod. 2π, when $\widetilde{\mathrm{KE}}$ is maximum) while $\widetilde{\mathrm{PE}}$ is forced twice (at $\Phi_0 - \pi/2$ and $\Phi_0 + \pi/2$, when $\widetilde{\mathrm{KE}} = \widetilde{\mathrm{PE}}$). $\widetilde{\mathrm{BF}}$ is positive when averaged over an RSS region, because $\widetilde{\mathrm{KE}}$ is transferred into $\widetilde{\mathrm{PE}}$ during the same time, and negative over a ISS region because $\widetilde{\mathrm{PE}}$ is transferred into $\widetilde{\mathrm{KE}}$ (ζ_0 changing sign to become negative). The ratio of $\widetilde{\mathrm{PEP}}$ to $\widetilde{\mathrm{BF}}$ when each quantity is averaged over a RSS region

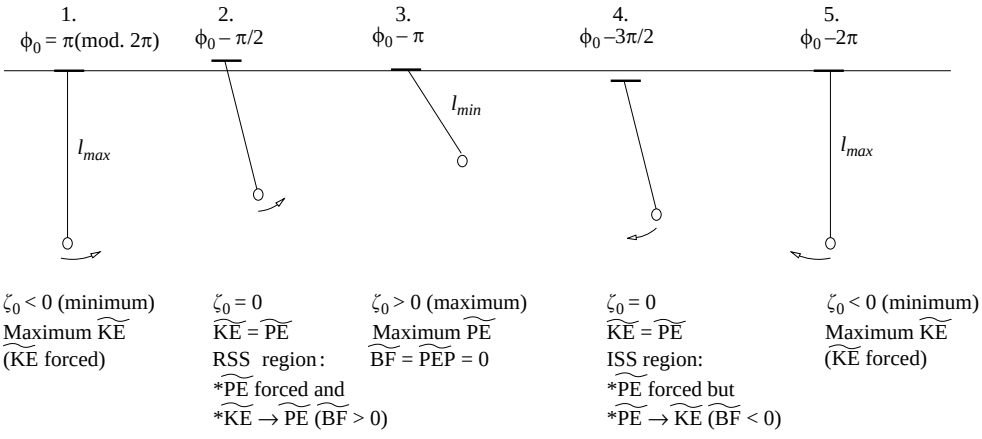

FIGURE 8. Sketch of the parametric forcing mechanism over one primary wave period, using an analogy with a parametrically forced pendulum. The motion of the pendulum is analogous to that of the resonant wave field at a fixed location in the fluid domain. Position 1 is the equilibrium position of the pendulum, where the kinetic energy $\widetilde{KE}$ is maximum. In the internal wave problem, forcing of $\widetilde{KE}$ occurs through the primary wave shear, and is identical to increasing the length l of the pendulum. At positions 2 and 4, a second forcing mechanism, now for the resonant wave potential energy $\widetilde{PE}$, occurs through the primary wave density gradient. Position 2 corresponds to an RSS region; in the pendulum analogy, its support rises (and the rising motion benefits from an apparent lower gravity); $\widetilde{KE}$ is moreover transferred into $\widetilde{PE}$ at that location so that the net rate of change of $\widetilde{PE}$ is positive. Position 4 corresponds to an ISS region; in the pendulum analogy, its supports goes down (so that the apparent gravity increases); $\widetilde{PE}$ is, however, transferred into $\widetilde{KE}$ at that location and, for the range of primary wave amplitudes we consider, the net rate of change of $\widetilde{PE}$ is always negative. Position 3 coincides with the maximum angular displacement of the pendulum and $\widetilde{PE}$ is therefore maximum at that position; the length of the pendulum is minimum there. ζ_0 is the vorticity of the primary wave and Φ_0 denotes its phase.

is equal to

$$\frac{\langle \widetilde{PEP} \rangle_{RSS}}{\langle \widetilde{BF} \rangle_{RSS}} = \frac{\pi}{4} \frac{\sin(\theta_1 - \theta_0)}{\cos\theta_1} \frac{A_0 \kappa_0^2}{N} \tag{24}$$

$$= \frac{\pi}{4} \frac{\sin(\theta_1 - \theta_0)}{\sin\theta_0 \cos\theta_1} s_0 \tag{25}$$

$$\simeq 1.29 s_0, \tag{26}$$

this quantity having an opposite sign for an ISS region. Thus, in RSS and ISS regions, the buoyancy flux dominates the potential (and kinetic as well) energy production terms as long as $s_0 < 0.77$, which is the case for all runs considered here (assuming the kinematic triad model remains reliable for such large values of s_0). It follows that the net rate of change of $\widetilde{PE}$ is positive in RSS regions only, being always negative in ISS regions. We shall see that, as the perturbation amplitude increases, the breakdown of the internal wave field is initiated in RSS regions through a secondary instability. The source of energy is therefore the potential energy of the primary wave, so that this instability must be a buoyancy-induced instability.

The chronology of these energy transfers is sketched in figure 8, using an analogy with a parametrically forced pendulum. The parametric instability is amplified because of two forcing mechanisms, namely the oscillation of the vertical density gradient of

the primary wave and of its vertical shear. In the pendulum analogy, the former mechanism is analogous to the vertical oscillation of the support of the pendulum and the latter, to the oscillation of the length of the pendulum. Each of these two forcing mechanisms implies a periodic modulation of the local frequency experienced by the perturbation, a process resulting in its parametric amplification. This analogy usefully complements that proposed by Bouruet-Aubertot *et al.* (1995).

6.3. *Results from the numerical simulations*

A global and frame independent view of the forcing mechanism as observed in the DNS can be gained by averaging KE′, PE′ and BF′, the quadratic terms for the perturbation, and KEP and PEP, the energy exchange terms between the primary wave and the perturbation, over the regions of the numerical domain where the primary wave vorticity ζ_0 is either positive or negative. The former region will be referred to as a P region and the average is denoted as $\langle\cdot\rangle_P$; the latter region will be referred to as a N region and the average is denoted as $\langle\cdot\rangle_N$. All averaged quantities are also normalized by the total energy of the perturbation. As previously, the same notation will be used to refer to a normalized and a non-normalized quantity.

For comparison purposes with the DNS results, the quadratic and energy production terms predicted by the triad model for triad T_1 have also been averaged over the P and N regions and normalized by the total energy of the resonant waves. An average over a P region simply amounts to integrating with respect to Φ_0, for $\Phi_0 \in [-\pi/2, \pi/2]$. For an N region, Φ_0 varies between $\pi/2$ and $3\pi/2$. It is assumed that Φ_1 varies much faster than Φ_0 so that the $\sin^2\Phi_1$ factor in these terms only contributes a factor of $1/2$ to the average.

6.3.1. *Results for run* 0

The steepness of the primary wave is small for run 0 (see table 1) and this case thus illustrates the weakly nonlinear regime. The temporal evolution of the quadratic and energy exchange terms computed from DNS for run 0 are displayed in figure 9. The DNS values obtained at $t = 40T_{BV}$ are compared in table 3 with the predictions of these terms by the triad model for triad T_1.

Since the primary wave is perturbed by a white noise, time is required for the resonant triads to emerge from that noise (and control the perturbation growth). As a consequence, an erratic behaviour occurs at early times, whose duration depends upon the primary wave amplitude.

The ratio of the domain-averaged perturbation kinetic energy $\langle \mathrm{KE}' \rangle$ to potential energy $\langle \mathrm{PE}' \rangle$ is plotted in figure 9(*a*) versus time (each quantity is displayed in figure 1(*b*) and has already been commented on in § 3). A unit value is predicted for this ratio by the triad model (see table 3) consistently with the model consisting of a superposition of linear internal gravity waves. Figure 9(*a*) however, shows that, in the DNS run 0, this ratio departs slightly from unity, $\langle \mathrm{KE}' \rangle$ being smaller than $\langle \mathrm{PE}' \rangle$ by less than 1 %.

The averaged values of KE′ and PE′ over the N and P regions are displayed in figure 9(*b*). Since kinetic (potential) energy in an N (P) region is converted into potential (kinetic) energy when this region becomes a P (N) region, we would expect $\langle \mathrm{KE}' \rangle_N = \langle \mathrm{PE}' \rangle_P$ ($\langle \mathrm{KE}' \rangle_P = \langle \mathrm{PE}' \rangle_N$) if exact equipartitioning between perturbation kinetic and potential energy were to occur. These equalities are indeed predicted by the triad model (see table 3). When the DNS results for this run are examined, figure 9(*b*) and table 3 show that $\langle \mathrm{KE}' \rangle_P = \langle \mathrm{PE}' \rangle_N$ also and the value matches that predicted by the triad model by 1 %. Figure 9(*b*),

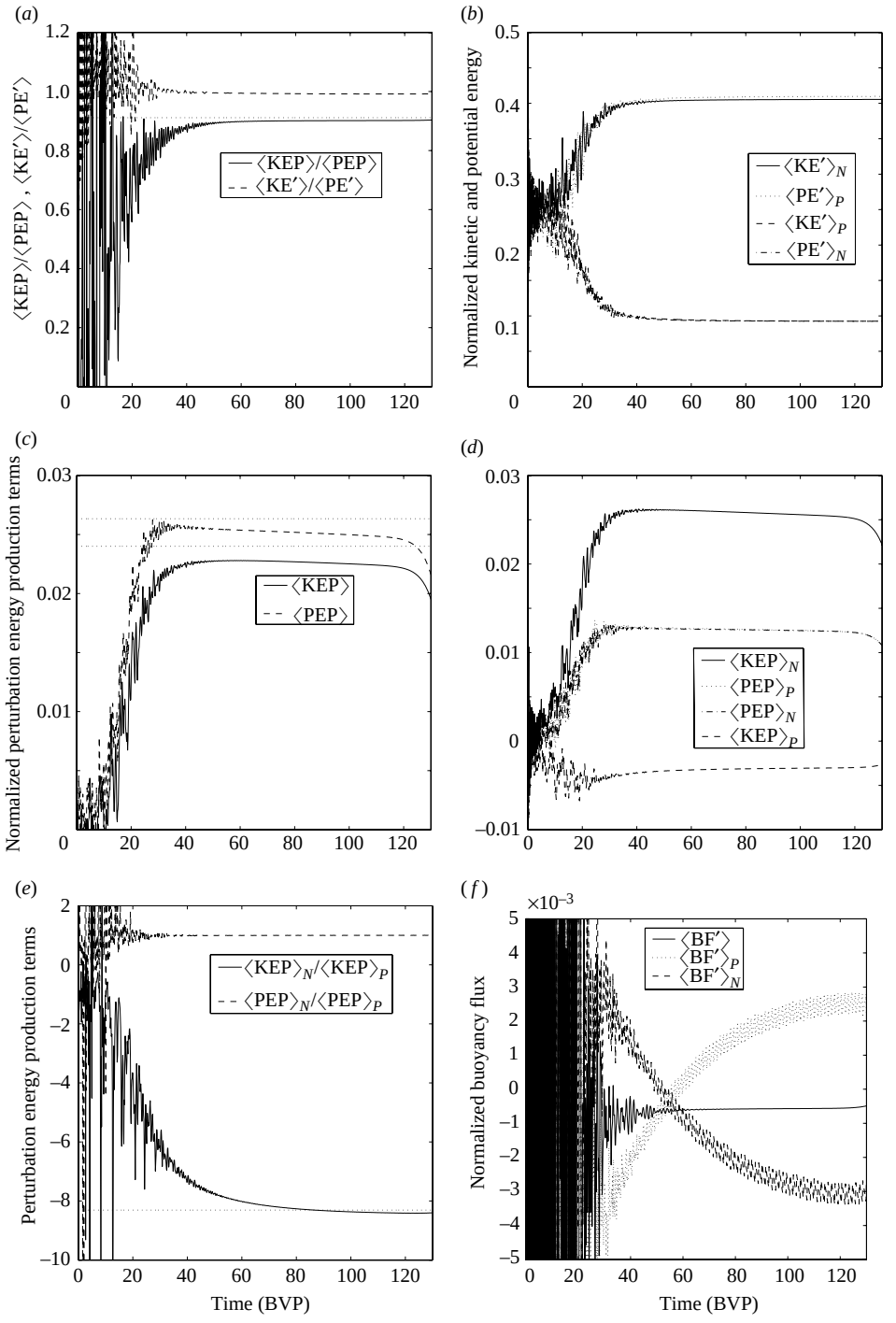

FIGURE 9. Energetics of destabilization for DNS run 0. KE′, PE′, BF′, KEP and PEP have been defined in § 6.1. These quantities are averaged either over the whole numerical domain ($\langle\ \rangle$) or over region where the primary wave vorticity is either negative ($\langle\ \rangle_N$) or positive ($\langle\ \rangle_P$). Comparison with the theoretical predictions by the triad model are displayed using a dotted line in (*a*) for $\langle \mathrm{KEP}\rangle/\langle \mathrm{PEP}\rangle$, in (*c*) for $\langle \mathrm{KEP}\rangle$ and $\langle \mathrm{PEP}\rangle$ (the theoretical values overestimating the numerical ones) and in (*e*) for $\langle \mathrm{KEP}\rangle_N/\langle \mathrm{KEP}\rangle_P$. All quantities are normalized by the instantaneous value of $\langle \mathrm{KE}'\rangle + \langle \mathrm{PE}'\rangle$.

1	2	3	4	5	6	7
$\widetilde{Q}$, Q'	$\frac{1}{2\pi}\int_{-\pi/2}^{\pi/2}\widetilde{Q}\,\mathrm{d}\Phi_0$	$\frac{1}{2\pi}\int_{-\pi/2}^{\pi/2}\widetilde{Q}\,\mathrm{d}\Phi_0$ for triad T_1	DNS value $\langle Q'\rangle_P$	$\frac{1}{2\pi}\int_{\pi/2}^{3\pi/2}\widetilde{Q}\,\mathrm{d}\Phi_0$	$\frac{1}{2\pi}\int_{\pi/2}^{3\pi/2}\widetilde{Q}\,\mathrm{d}\Phi_0$ for triad T_1	DNS value $\langle Q'\rangle_N$
$\widetilde{\mathrm{KE}}$, KE′	$\frac{1}{4}-\frac{1}{2\pi}$	$\frac{1}{4}-\frac{1}{2\pi}$	0.092	$\frac{1}{4}+\frac{1}{2\pi}$	$\frac{1}{4}+\frac{1}{2\pi}$	0.405
$\widetilde{\mathrm{PE}}$, PE′	$\frac{1}{4}+\frac{1}{2\pi}$	$\frac{1}{4}+\frac{1}{2\pi}$	0. 409	$\frac{1}{4}-\frac{1}{2\pi}$	$\frac{1}{4}-\frac{1}{2\pi}$	0.092
$\widetilde{\mathrm{BF}}$, BF′	0	0	$-4.1\ 10^{-3}$	0	0	2.9×10^{-3}
$\widetilde{\mathrm{KEP}}$, KEP	$\left(\frac{1}{8}-\frac{1}{2\pi}\right)A\kappa_0^2\times\sin[2(\theta_1-\theta_0)]$	−0.0035	−0.0035	$\left(\frac{1}{8}+\frac{1}{2\pi}\right)A\kappa_0^2\times\sin[2(\theta_1-\theta_0)]$	0.029	0.026
$\widetilde{\mathrm{PEP}}$, PEP	$\frac{1}{4}A\kappa_0^2\sin(\theta_1-\theta_0)$	0.014	0.013	$\frac{1}{4}A\kappa_0^2\sin(\theta_1-\theta_0)$	0.014	0.013

TABLE 3. Quadratic and energy exchange terms for run 0. Comparison between (i) the predictions of these terms by the triad model (tilde terms) for triad T_1 and (ii) their DNS values at $t = 40\ T_{BV}$ (primed terms, KEP, PEP). All terms are normalized by the energy of the perturbation and are averaged over a region where the primary wave vorticity is either positive (columns 2, 3 and 4) or negative (columns 5, 6 and 7). Analytical predictions by the triad model are indicated in columns 2 and 5. The values of these predictions for triad T_1 are indicated in columns 3 and 6. The DNS values are indicated in columns 4 and 7.

however, shows that $\langle \mathrm{KE}'\rangle_N$ is slightly smaller than $\langle \mathrm{PE}'\rangle_P$, which accounts for the finding in figure 9(*a*). The value for $\langle \mathrm{PE}'\rangle_P$ is predicted well by the triad model implying that the unexpected discrepancy between $\langle \mathrm{KE}'\rangle$ and $\langle \mathrm{PE}'\rangle$ lies in $\langle \mathrm{KE}'\rangle_N$.

The ratio of $\langle \mathrm{KEP}\rangle$ to $\langle \mathrm{PEP}\rangle$ is displayed in figure 9(*a*). As opposed to the perturbation energy ratio, $\langle \mathrm{KEP}\rangle/\langle \mathrm{PEP}\rangle$ is clearly different from 1. This means that the transfer of potential energy from the primary wave to the perturbation is larger than the transfer of kinetic energy from that wave. This behaviour is intrinsic to internal gravity wave dynamics; indeed, the triad model predicts that

$$\frac{\langle \widetilde{\mathrm{KEP}}\rangle}{\langle \widetilde{\mathrm{PEP}}\rangle} = \cos(\theta_1-\theta_0), \tag{27}$$

(see table 3), that is, it depends only upon the angle that the primary wave vector makes with the horizontal (since $\cos\theta_1 = 0.5\cos\theta_0$). This expression, theoretically valid in the limit of infinitely small primary wave amplitude, approximates quite well the value found in the DNS, the relative difference being only 5 %.

The domain-averaged energy production terms $\langle \mathrm{KEP}\rangle$ and $\langle \mathrm{PEP}\rangle$ are plotted in figure 9(*c*), along with their predictions by the triad model. These predictions match quite closely the DNS findings, the prediction for $\langle \mathrm{PEP}\rangle$ being better than for $\langle \mathrm{KEP}\rangle$ (the relative errors are ~ 2 % and ~ 5 %, respectively). The averaged value of KEP and PEP over the N and P regions is displayed in figure 9(*d*), the ratios $\langle \mathrm{KEP}\rangle_N/\langle \mathrm{KEP}\rangle_P$ and $\langle \mathrm{PEP}\rangle_N/\langle \mathrm{PEP}\rangle_P$ being displayed in figure 9(*e*). As indicated in table 3, the triad model also provides a good approximation of these four averaged quantities (apart from a small overestimation of $\langle \mathrm{KEP}\rangle_N$) so that their ratios are also predicted well. These results can be interpreted with the triad model: since perturbation potential energy is forced twice per primary wave period (in RSS and ISS regions), one expects

$\langle \mathrm{PEP} \rangle_P = \langle \mathrm{PEP} \rangle_N$, which is indeed found. By contrast, since perturbation kinetic energy is forced once, in an N region, one expects $\langle \mathrm{KEP} \rangle_N$ to be much larger than $\langle \mathrm{KEP} \rangle_P$. The relative magnitude of the two latter terms is provided by the triad model and is equal to $|(2\pi + 8)/(2\pi - 8)| \simeq 8.32$.

Since $\langle \mathrm{PEP} \rangle$ is larger than $\langle \mathrm{KEP} \rangle$, but $\langle \mathrm{KE}' \rangle \simeq \langle \mathrm{PE}' \rangle$, a net transfer of perturbation potential energy into perturbation kinetic energy should occur over a primary wave period. Hence, the perturbation buoyancy flux $\langle \mathrm{BF}' \rangle$ should be negative to maintain the equipartition between $\langle \mathrm{KE}' \rangle$ and $\langle \mathrm{PE}' \rangle$. This equipartition is indeed a vital condition to sustain the efficiency of energy transfers from the primary wave (that is, to sustain the instability itself). Since $\langle \mathrm{PE}' \rangle$ is transferred into $\langle \mathrm{KE}' \rangle$ in an N region and $\langle \mathrm{KE}' \rangle$ into $\langle \mathrm{PE}' \rangle$ in a P region, $\langle \mathrm{BF}' \rangle_N$ (which is negative) should have a larger absolute value than $\langle \mathrm{BF}' \rangle_P$. Figure 9($f$) confirms this interpretation.

In this discussion, some discrepancies have been noted between the predictions by the triad model and DNS findings. Thus, the ratio $\langle \mathrm{KEP} \rangle_N / \langle \mathrm{KEP} \rangle_P$ is lower by 10 % than the theoretical prediction, owing to the discrepancy between the prediction of $\langle \mathrm{KEP} \rangle_N$ by the triad model and its DNS value. Assuming that the triad model prediction is correct, this discrepancy indicates that the kinetic energy forcing in the DNS is not as efficient as it could be. This may already be a manifestation of the finite amplitude of the primary wave and would account for $\langle \mathrm{KE}' \rangle_N$ being smaller than $\langle \mathrm{PE}' \rangle_P$ in figure 9(b). Finally, we should stress that the triad model has limitations. Thus, the negativity of the buoyancy flux is not predicted by the model. This is because σ' is derived for each resonant wave of the triad from the polarization relation for an unforced wave. The error in the prediction of the numerical value of $\langle \mathrm{BF}' \rangle$ is actually within the range of the other relative errors of the model predictions, but it exposes the limitation of a kinematic model.

6.3.2. *Results for runs* 2 *and* 3

The primary wave amplitude has been increased by a factor 4 in run 2 (figure 10) and by a factor 16 in run 3 (not shown). We recover the striking feature just described for run 0: potential energy transfer from the primary wave ($\langle \mathrm{PEP} \rangle$) is greater than kinetic energy transfer from that wave ($\langle \mathrm{KEP} \rangle$), but perturbation kinetic and potential energy remain roughly equipartitioned (to sustain the instability) so that the net buoyancy flux is negative.

Figure 10 also shows that all quantities related to potential energy are predicted well by the kinematic model. Since this model is strictly valid for infinitely small primary wave amplitude, we attribute all differences with its predictions to the increase in amplitude of the primary wave, as for run 0. The main effect, already guessed in run 0, is that the efficiency of the kinetic energy transfer from the primary wave, which occurs in an N region, decreases as A_0 increases. Figure 6 provides a possible mechanism to account for this behaviour: the phase lines of the perturbation in an N region lie partly outside this region, probably because of primary wave advection. Hence, the phase between the perturbation and the primary wave is modified in an N region, which decreases the efficiency of the kinetic energy transfer process. This phase modification may account for all quantities in figure 10 oscillating at the primary wave period.

This advection process in an N region is probably responsible for $\langle \mathrm{PEP} \rangle$ now being underpredicted by the triad model. In other words, the efficiency in potential energy extraction from the primary wave increases with the primary wave amplitude. Figure 6 may again be invoked to account for this behaviour; we already observed that the tail of the vorticity layers associated with the perturbation field is nearly horizontal (an

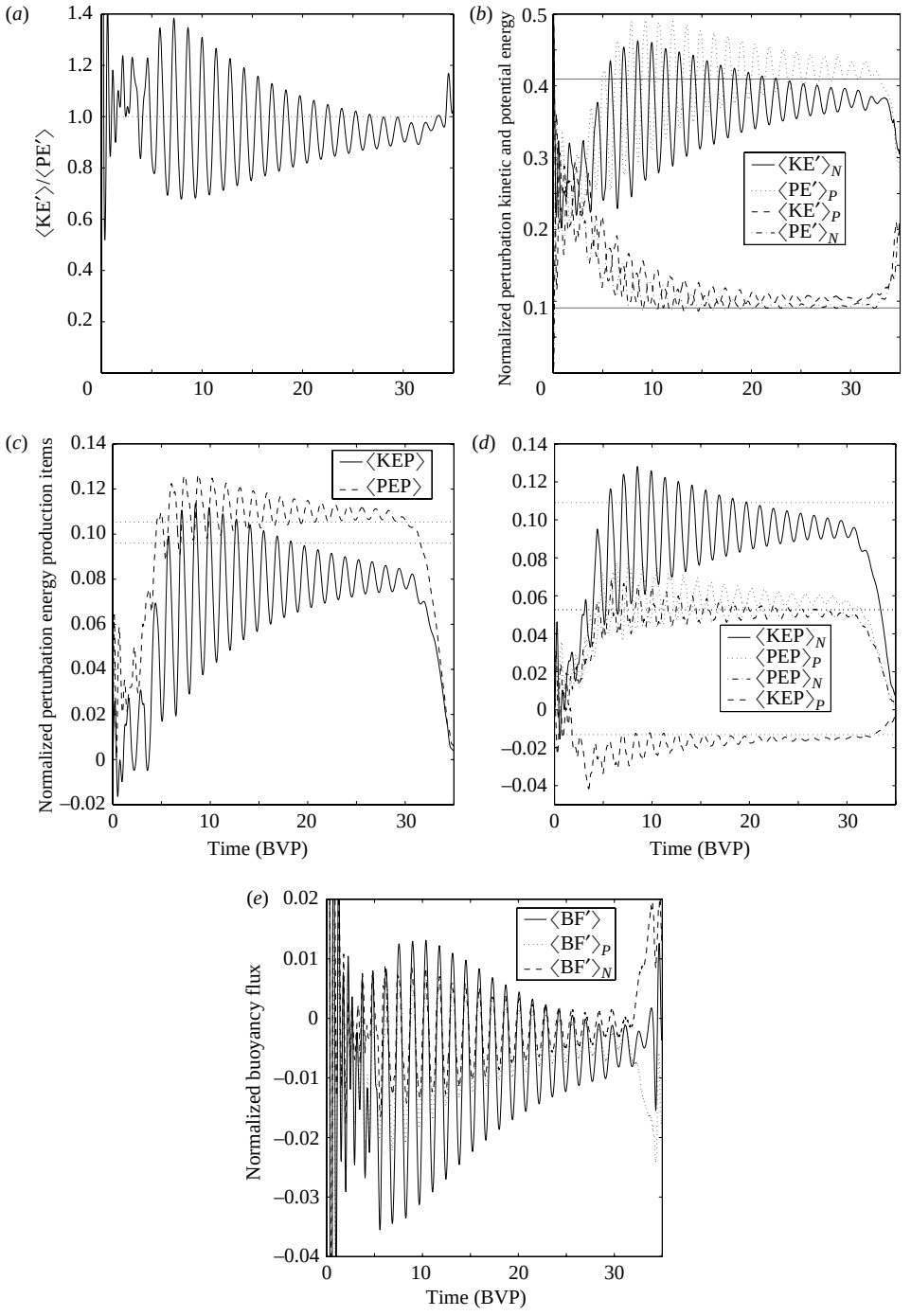

FIGURE 10. Energetics of destabilization for DNS run 2. A similar analysis to figure 9 is displayed. Comparison with the triad model predictions are displayed in (*a*)–(*d*) using a dotted line (except in (*b*)) where a full line is used for clarity). (*b*) Upper line: $\langle \mathrm{KE}' \rangle_N = \langle \mathrm{PE}' \rangle_P$, lower line: $\langle \mathrm{KE}' \rangle_P = \langle \mathrm{PE}' \rangle_N$. (*c*) Upper line: $\langle \mathrm{KEP} \rangle$; lower line: $\langle \mathrm{PEP} \rangle$. (*d*) Upper line: $\langle \mathrm{KEP} \rangle_N$, middle line: $\langle \mathrm{PEP} \rangle_N = \langle \mathrm{PEP} \rangle_P$, lower line: $\langle \mathrm{KEP} \rangle_P$. In all frames, quantities are normalized by the instantaneous value of $\langle \mathrm{KE}' \rangle + \langle \mathrm{PE}' \rangle$.

effect which we attributed to the finite amplitude of the primary wave field). These quasi-horizontal tails are in an RSS region, where isopycnal lines make the sharpest angle to the horizontal. We may consider the extreme case of a large-amplitude primary wave having almost vertical isopycnal lines. In RSS regions, the direction of particle motions tends to be quasi-orthogonal to the isopycnals, resulting in a penetration of light fluid under dense fluid, which increases the potential energy of the perturbation.

A further increase in the primary wave amplitude simply exacerbates these features (run 3, not shown). The approximate equipartition between $\langle \mathrm{KE}' \rangle$ and $\langle \mathrm{PE}' \rangle$ still holds, but now, both $\langle \mathrm{PEP} \rangle$ and $\langle \mathrm{KEP} \rangle$ strongly depart from the model prediction, the former rate being 50 % larger than the model prediction while the latter is twice too low. The buoyancy flux is now negative in both N and P regions to make up for the strong imbalance between kinetic and potential energy transfers from the primary wave.

In summary, runs 2 and 3 show that the basic mechanism of the parametric instability process is preserved when the wave amplitude increases, it being modified, but not destroyed, by the finite amplitude of the primary wave.

7. Breakdown of the wave field

In this section, we infer from simple considerations that the total wave field becomes locally unstable through a buoyancy-induced instability, as a result of the amplification of the perturbation by parametric instability. A Kelvin–Helmholtz instability may also develop, but we show from the triad model that, when amplification occurs, the growth rate of the buoyancy-induced instability is always larger than that of the Kelvin–Helmholtz instability.

7.1. *On the occurrence of a buoyancy-induced instability*

It was shown in § 6.2 that the net rate of change of perturbation potential energy is positive in RSS regions; consequently, if overturning is to occur in the fluid, it should occur in such regions. On the other hand, the maximum vorticity of the perturbation increases in $\zeta_0 < 0$ regions so that a Kelvin–Helmholtz instability may occur there.

The total density field is displayed at successive times in figure 11 for run 2. Figure 11(*a*) reveals that the density contours start deforming in RSS regions, as a result of the perturbation amplification. Figure 11(*b*) shows that, one primary wave period later, no Kelvin–Helmholtz instability is visible yet and that the regions of maximum kinetic energy of the perturbation (N region) still display unperturbed density lines. By contrast, statically unstable layers are forming in the RSS regions. Hence, the breaking of the total wave field should occur through a buoyancy-induced instability arising in RSS regions, as a result of the parametric amplification of the perturbation by the primary wave. Thus, the mechanisms underlying the development of the buoyancy-induced instability do not depend upon the primary wave amplitude.

7.2. *Kelvin–Helmholtz versus buoyancy-induced instability*

The internal wave breakdown event is initiated by the set of statically unstable layers, as shown in the preceeding paragraph. In our two-dimensional simulations, the subsequent development of wave breakdown actually results from Kelvin–Helmholtz instability (see figure 11*c*). The reason for this behaviour is the following. As shown by Thorpe (1994) and Batchelor & Nitsche (1991), a linear background stratification and a vertical shear tend to stabilize unstable layers. No shear exists in the direction transverse to the primary plane wave and laboratory experiments, both of breaking

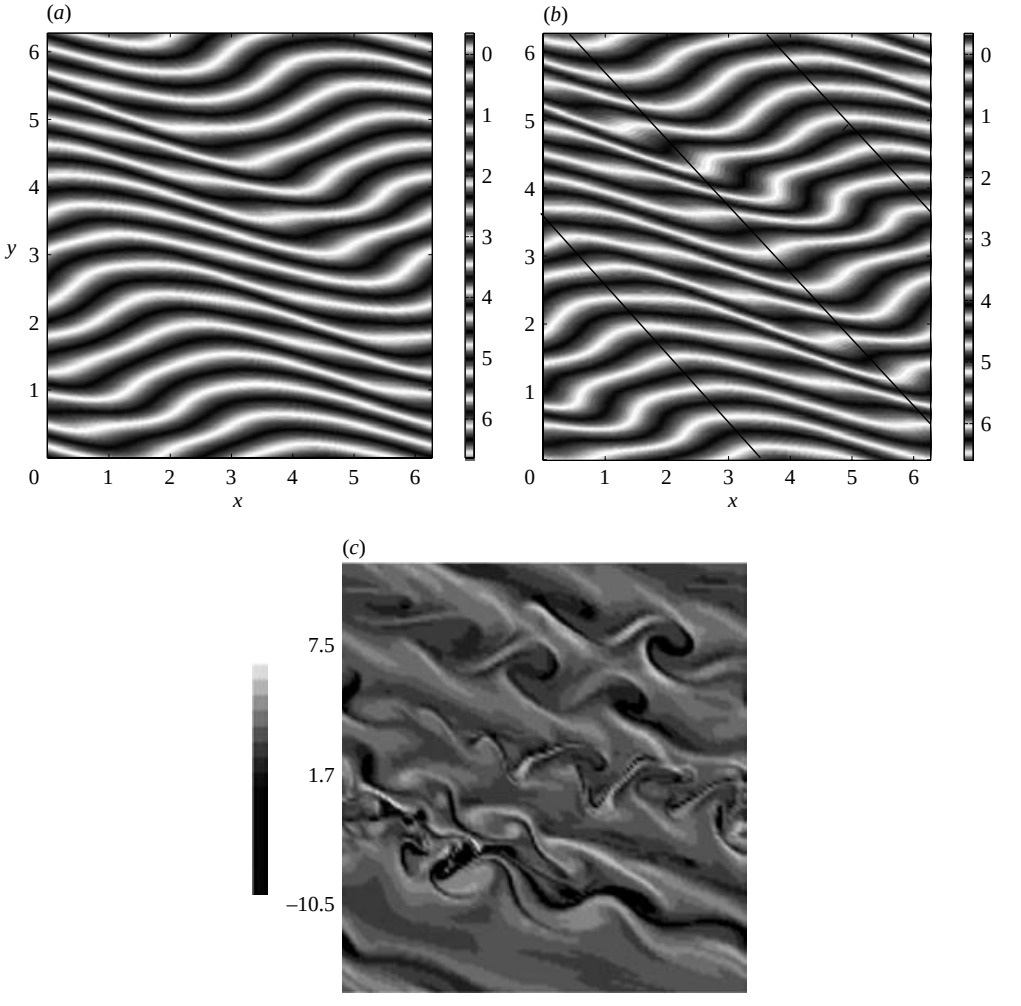

FIGURE 11. DNS results for run 2. Total density field at (*a*) $t = 20.5$ PWP, (*b*) $t = 21.4$ PWP in units of the primary wave period (PWP). The three black lines mark the approximate locations where ζ_0 is minimum (lower and upper lines) and maximum (middle line), so that the RSS regions can be inferred (see figure 5). (*c*) Total vorticity field for run 2 at 25.9 PWP (that is, 36.6 BVP).

gravity waves (Benielli & Sommeria 1998) and of a stably-stratified shear layer (Schowalter, Van Atta & Lasheras 1994) have shown that the buoyancy-induced instability does develop in this transverse direction. It is therefore an intrinsically three-dimensional instability. Consequently, the buoyancy-induced instability cannot develop in a two-dimensional plane simulation and the Kelvin–Helmholtz instability is promoted.

Let us show that a Kelvin–Helmholtz instability is not expected to occur in a three-dimensional fluid. For this purpose, we first estimate the growth rate of this instability. We introduce the local Richardson number $Ri(\boldsymbol{x}, t)$, defined as

$$Ri(\boldsymbol{x}, t) = \frac{N^2 - \partial\rho'/\partial z}{(\partial u/\partial z)^2} \tag{28}$$

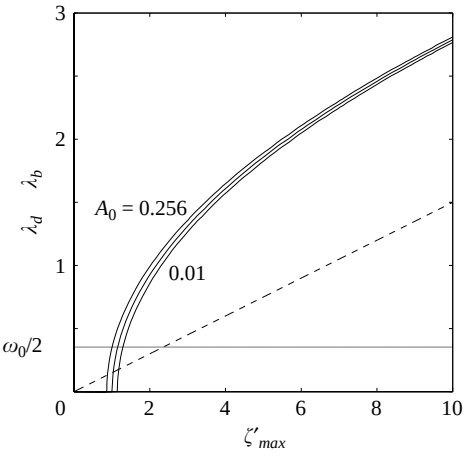

FIGURE 12. Growth rate of the buoyancy-induced instability λ_b defined by (30) for three values of the primary wave amplitude A_0 (full line) and of the dynamical (Kelvin–Helmholtz) instability λ_d defined by (29) for $\alpha = 0.15$ (dashed line), as a function of the maximum vorticity of the perturbation ζ'_{max}. The linear frequency of the parametrically forced perturbation $\omega_0/2$ is indicated with a horizontal full line.

where the numerator is the total vertical density gradient. A necessary condition for Kelvin–Helmholtz instability is that $Ri < 0.25$ somewhere (e.g. Drazin & Reid 1981), but this applies rigorously only to a plane parallel steady horizontal shear layer. It may be applied in the present case if the growth rate of the Kelvin–Helmholtz instability, λ_d say, is larger than the frequency of the vorticity layers (meaning that the instability has time to develop before the vorticity of the layers changes sign): $\lambda_d > \omega_0/2$. The growth rate of the Kelvin–Helmholtz instability is of the form

$$\lambda_d = \alpha(Ri)\zeta'_{max}, \tag{29}$$

where $\alpha(Ri)$ varies continuously from a value of $\simeq 0.2$ for $Ri \ll 1$ down to 0 if the Richardson number exceeds 1/4 everywhere (Hazel 1972); $\zeta'_{max} = 2A'\kappa_1^2$ denotes the maximum vorticity over the computational domain of the perturbation field. The Kelvin–Helmholtz instability may therefore develop if ζ'_{max} is larger than $\omega_0/(2\alpha)$.

Though this instability develops when the perturbation field has grown to appreciable amplitude, let us estimate α from the triad model by computing the local Richardson number in the region where the instability is expected to grow. This is where ζ_0 reaches its minimum value, that is for $\Phi_0 = \pi$ mod. 2π. In this region, the minimum value of Ri is $N^2/(\zeta_{0,max} + \zeta'_{max})^2$. At the time the instability develops, ζ'_{max} is larger than 5 for run 2 (while $\zeta_{0,max} = 0.256$) so that the minimum value of Ri is $\simeq N^2/(\zeta'_{max})^2$, which is much smaller than 1. Hence, $\alpha \simeq 0.2$. The condition $\zeta'_{max} > \omega_0/(2\alpha)$ therefore yields $\zeta'_{max} > 1.8$, which is satisfied. Hence, a Kelvin–Helmholtz instability might develop.

We now compare the growth rate of this instability with the buoyancy-induced instability growth rate, which we denote as λ_b. The maximum growth rate of the buoyancy-induced instability is $\lambda_b = \sqrt{-N^2 + \partial\rho'/\partial z}$ and is obtained in the limit of infinitely large wavenumbers (e.g. Drazin & Reid 1981). Let us compute an (approximate but explicit) estimate of λ_b from the triad model. We obtain,

$$\lambda_b^2 = -N^2 + \partial\Sigma_0/\partial z + \partial\sigma'/\partial z$$
$$= -N^2 + \zeta_{0,max} N \sin\theta_0 \sin\Phi_0 + \zeta'_{max} N \sin\theta_1 \cos\left(\tfrac{1}{2}\Phi_0\right) \sin\Phi_1. \quad (30)$$

It can be shown from this relation that, as the perturbation amplifies, a positive value for λ_b^2 is first reached for a value of Φ_0 varying from 0 to $\pi/2$, as the primary wave amplitude increases (assuming $\sin\Phi_1 = 1$) that is, in a RSS region. As for the Kelvin–Helmholtz instability, λ_b has to be larger than $\omega_0/2$ for the buoyancy-induced instability to be able to develop there. This implies that, for instance, $\zeta'_{max} > 1.20$ for run 0 and $\zeta'_{max} > 1$ for run 2.

The growth rates λ_d and λ_b are plotted versus ζ'_{max} in figure 12, along with the frequency $\omega_0/2$. λ_d is plotted for $\alpha = 0.15$, corresponding to a minimum value of the Richardson number equal to $\simeq 0.06$; λ_b is plotted for three different amplitudes of the primary wave: $A_0 = 0.01$, which illustrates the asymptotic behaviour $A_0 \to 0$, $A_0 = 0.128$ and $A_0 = 0.256$ (we set $\sin\Phi_1 = 1$ and $\Phi_0 = \pi/4$). Figure 12 shows that when λ_d exceeds $\omega_0/2$, λ_b is always larger than λ_d and their relative magnitude increases as A_0 increases. We thus recover the result that buoyancy-induced instability is more likely to develop than Kelvin–Helmholtz instability for a high-frequency wave (e.g. Munk 1981) and quantitative and physical supports to this result are provided by the present study.

It should be pointed out that the behaviour displayed in figure 12 is valid in the inviscid limit while the growth rates λ_d and λ_b are associated with instability at a very different scale. The buoyancy-induced instability is most sensitive to viscous effects (like the parametric instability), as opposed to the Kelvin–Helmholtz instability. Hence, if viscous effects are strong enough to damp the former instability, Kelvin–Helmholtz instability will dominate. Only in this case would two-dimensional simulations be appropriate for investigating the complete flow dynamics.

8. Summary and conclusion

This study has provided a detailed investigation of the instability mechanism for an internal gravity wave of high frequency (termed the primary wave). Resonant interaction theory has been used for this purpose and we have developed a kinematic model of the resonant waves excited by the primary wave to investigate the spatio-temporal organization of the energy transfers from the primary wave. We showed that parametric instability may be viewed as an optimum scenario for extracting energy from the primary wave. Numerical simulations performed in a vertical plane have permitted us to validate the kinematic model for a weak steepness primary wave. We next used the simulations and the model to study the instability dynamics as the primary wave amplitude increases and to investigate the breaking process of the wave field.

From resonant interaction theory and numerical simulations, we concluded that a few resonant secondary waves with close wave vectors are amplified. They grow at nearly identical rates and can be assumed to be independent, at least during the early stage of the amplification process. The scale of these resonant waves is selected by molecular effects and by the grid size. Only one value of the Prandtl number was considered in this study ($Pr = 1$), but the expression of the linear damping factor of the growth rate of the resonant waves in § 4.2 shows that increasing the Prandtl number has the same effect as decreasing the viscosity. Hence, higher secondary wavenumbers should be selected when the Prandtl number is increased.

These results set the basis of the kinematic model to investigate how a perturbation amplifies in space and time through parametric instability: the perturbation growth is assumed to be controlled by a few independent triads of close geometry and, therefore, only one of them need be considered to model the energy exchange with the primary wave. The assumptions of the model are that the resonant waves of the triad are of small scale relative to the primary wave; the phase relation between the primary and the secondary waves is inferred from the numerical simulations.

It has been shown previously (e.g. Lombard & Riley 1996*a*) that the parametric forcing of the perturbation field occurs through two mechanisms. (i) The perturbation kinetic energy KE′ is forced through the shear of the primary wave (as for any steady shear flow instability). We show here that the oscillating shear of the primary wave strongly constrains the perturbation field, at a given location in the numerical domain: its energy is under kinetic form when the primary wave shear is negative, which maximizes the transfer from that wave, and is stored under potential form when the primary wave shear is positive, which minimizes the reverse transfer to that wave. Hence, the perturbation kinetic energy has the same phase as the primary wave vorticity. (ii) The perturbation potential energy PE′ is forced through the density gradient of the primary wave. We show that this forcing occurs twice per primary wave period, when the latter gradient is either positive (this occurs in a region of reduced static stability, RSS for short) or negative (increased static stability region, ISS for short). These two stages are, however, not symmetric: perturbation kinetic energy KE′ is transferred into potential energy PE′ in the RSS region, resulting in a positive rate of change for PE′ while the reverse transfer in the ISS region results in a negative rate of change for PE′.

A fundamental result of our study is that the transfer rate of potential energy from the primary wave to the perturbation $\langle \mathrm{PEP} \rangle$ is larger than the transfer rate of kinetic energy $\langle \mathrm{KEP} \rangle$ whatever the primary wave. Indeed, the ratio of $\langle \mathrm{KEP} \rangle$ to $\langle \mathrm{PEP} \rangle$ predicted by the model is equal to $\cos(\theta_1 - \theta_0)$ with $\cos\theta_1 = 0.5\cos\theta_0$. This ratio decreases to 1/2 for a very high-frequency primary wave ($\theta_0 \to 0$); such a decrease is intuitively expected since motions induced by the primary wave are nearly vertical. It increases to 1 for a very low-frequency primary wave ($\theta_0 \to \pi/2$); in a geophysical context; however, Coriolis effects should be taken into account which would increase the kinetic energy of the primary wave and thus modify the analysis.

This behaviour shows that potential energy transfer from an unstable primary wave of small amplitude is easier than kinetic energy transfer. This is a very general result, which has already been observed in stratified turbulence (e.g. Holloway & Ramsden 1988) and when the linear stability of a three-dimensional internal gravity wave is studied (Lombard & Riley 1996*a*). In stratified turbulence, this behaviour implies that potential energy is transferred more efficiently than kinetic energy toward small scales. The same implication holds here since parametric instability transfers energy (directly, without cascade process, as noted by Pierrehumbert 1986) from the large-scale primary wave down to the small-scale secondary waves. According to Holloway & Ramsden (1988), the subset of two-dimensional interactions in a three-dimensional field might be responsible for this behaviour, since the nonlinear conservation of enstrophy in two dimensions prevents kinetic energy from being transferred toward small scales. The incompressibility constraint, which applies to the velocity field, but not to the density field, may also account for this behaviour (Lesieur 1997).

The excess of perturbation potential energy to kinetic energy is compensated for by a negative buoyancy flux to ensure the equipartitioning between these two forms

of energy. This equipartition is necessary to maintain the efficiency of the instability process. This implies that a counter-gradient buoyancy flux occurs at small scales, as also noted by Holloway & Ramsden (1988) for stratified turbulence.

As in Lombard & Riley (1996*a*), we observe that this imbalance in energy extraction increases with the primary wave amplitude. Our detailed study shows that this is because kinetic energy transfer (in the $\zeta_0 < 0$ region) loses efficiency relative to the optimum transfer (which occurs for infinitely small primary wave amplitude). Moreover, as the primary wave amplitude increases further, the potential energy transfer from the primary wave becomes more efficient which reinforces this imbalance.

Our computations show that, as expected, overturning occurs first (in time) in RSS regions. Hence, the total wave field should eventually become unstable in these regions to a (three-dimensional small-scale) buoyancy-induced instability, as a result of the parametrically forced perturbation. The wave field may also be unstable through a (two-dimensional large-scale) dynamical instability of the Kelvin–Helmholtz type in the $\zeta_0 < 0$ region, where the kinetic energy of the perturbation is maximum. In our two-dimensional computations, breaking eventually occurs through Kelvin–Helmholtz instability, but we conclude that, unless viscous effects are strong enough, this route to breaking is selected by the two-dimensional geometry. Hence, the final breaking stage of the flow cannot be studied in a reliable manner with two-dimensional simulations. This three-dimensional breaking process is well known to occur when the steepness of the primary wave exceeds 1 (Winters & Riley 1992; Winters & D'Asaro 1994; Andreassen *et al.* 1998) whatever its frequency (Lelong & Dunkerton 1998*b*). We showed here that this result also holds for a vanishingly small primary wave steepness, when its frequency is high enough.

We thank M. McIntyre for helpful discussions. The simulations were performed on the computers of IDRIS (CNRS High Performance Computer Center).

REFERENCES

Andreassen, O., Hvidsten, P. O., Fritts, D. C. & Arendt, S. 1998 Vorticity dynamics in a breaking internal gravity wave. Part 1. Initial instability evolution. *J. Fluid Mech.* **367**, 27–46.

Batchelor, G. K. & Nitsche, J. M. 1991 Instability of stationary unbounded stratified fluid. *J. Fluid. Mech.* **227**, 357–391.

Benielli, D. & Sommeria, J. 1998 Excitation and breaking of internal gravity waves by parametric instability. *J. Fluid Mech.* **374**, 117–144.

Bouruet-Aubertot, P., Sommeria, J. & Staquet, C. 1995 Breaking of standing internal gravity waves through two-dimensional instabilities. *J. Fluid Mech.* **285**, 265–301.

Canuto, C., Hussaini, M., Quateroni, A. & Zang, T. A. 1988 *Spectral Methods in Fluid Dynamics.* Springer.

Carnevale, G. F. & Martin, P. C. 1982 Field theoretical techniques in statistical fluid dynamics: with application to nonlinear wave dynamics. *Geophys. Astrophys. Fluid Dyn.* **20**, 131–164.

Chen, C. Y. & Holloway, G. 1986 A numerical study of the frequency and energetics of nonlinear internal gravity waves. *J. Geophys. Res.* **91**, 953–973.

Chow, C. C., Henderson, D. & Segur, H. 1996 A generalized stability criterion for resonant triad interactions. *J. Fluid Mech.* **319**, 67–76.

Craik, A. D. D. 1985 *Wave Interactions and Fluid Flow*. Cambridge University Press.

Cushman-Roisin, B. 1994 *Introduction to Geophysical Fluid Dynamics.* Prentice-Hall.

Davis, R. E. & Acrivos, A. 1967 The stability of oscillatory internal waves. *J. Fluid Mech.* **30**, 723–736.

Drazin, P. G. 1977 On the parametric instability of an internal gravity wave. *Proc. R. Soc. Lond.* A **356**, 411.

Drazin, P. G. & Reid, W. H. 1981 *Hydrodynamic Stability*. Cambridge University Press.

Frederiksen, J. S. & Bell, R. C. 1983 Statistical dynamics of internal gravity waves-turbulence. *Geophys. Astrophys. Fluid Dyn.* **26**, 257–301.

Frederiksen, J. S. & Bell, R. C. 1984 Energy and entropy evolution of interacting gravity waves and turbulence. *Geophys. Astrophys. Fluid Dyn.* **28**, 171–203.

Gill, A. E. 1982 *Atmosphere-Ocean Dynamics*. Academic.

Hasselmann, K. 1967 A criterion for nonlinear wave stability. *J. Fluid Mech.* **30**, 737–739.

Hazel, P. 1972 Numerical studies of the stability of inviscid stratified shear flows. *J. Fluid Mech.* **51**, 39–61.

Holloway, G. 1979 On the spectral evolution of nonlinear interacting waves. *Geophys. Astrophys. Fluid Dyn.* **11**, 271–287.

Holloway, G. & Ramsden, D. 1988 Theories of internal wave interaction and stably stratified turbulence: testing against numerical simulations. In *Small-scale Turbulence and Mixing in the Ocean* (ed. J. C. Nihoul & B. M. Jamard), Aha Huliko'a Hawaiian Winter Workshop, pp. 363–377. Elsevier.

Klostermeyer, J. 1982 On parametric instabilities of finite-amplitude internal gravity waves. *J. Fluid Mech.* **119**, 367–377.

Klostermeyer, J. 1991 Two and three-dimensional parametric instabilities in finite amplitude internal gravity waves. *Geophys. Astrophys. Fluid Dyn.* **61**, 1.

Leblanc, S. 2003 Internal wave resonances in strain flows. *J. Fluid Mech.* **477**, 259–283.

Lelong, M. P. & Dunkerton, T. J. 1998*a* Inertia-gravity waves breaking in three dimensions: 1. Convectively stable waves. *J. Atmos. Sci.* **55**, 2473.

Lelong, M. P. & Dunkerton, T. J. 1998*b* Inertia-gravity wavesbreaking in three dimensions: 2. convectively unstable waves. *J. Atmos. Sci.* **55**, 2489.

Lesieur, M. 1997 *Turbulence in Fluids*, 3rd edn. Kluwer.

Lombard, P. N. & Riley, J. J. 1996*a* Instability and breakdown of internal gravity waves. I. linear stability analysis. *Phys. Fluids* **8**, 3271.

Lombard, P. N. & Riley, J. J. 1996*b* On the breakdown into turbulence of propagating internal waves. *Dyn. Atmos. Oceans* **24**, 345–356.

McEwan, A. D. 1971 Degeneration of resonantly-excited standing internal gravity waves. *J. Fluid Mech.* **50**, 431–448.

McEwan, A. D., Mander, D. W. & Smith, R. K. 1972 Forced resonant second-order interaction between damped internal waves. *J. Fluid Mech.* **55**, 589–608.

McEwan, A. D. & Plumb, R. A. 1977 Off-resonant amplification of finite internal wave packets. *Dyn. Atmos. Ocean* **2**, 83–105.

McEwan, A. D. & Robinson, R. M. 1975 Parametric instability of internal gravity waves. *J. Fluid Mech.* **67**, 667–687.

Majda, A. J. & Shefter, M. G. 1998 Elementary stratified flows with instability at large Richardson number. *J. Fluid Mech.* **376**, 319–350.

Martin, S., Simmons, W. & Wunsch, C. 1972 The excitation of resonant triads by single internal waves. *J. Fluid Mech.* **53**, 17–44.

Mied, R. P. 1976 The occurence of parametric instabilities in finite-amplitude internal gravity waves. *J. Fluid Mech.* **78**, 763–784.

Miyazaki, T. & Adachi, K. 1998 Short-wavelength instabilities of waves in rotating stratified fluids. *Phys. Fluids* **10**, 3168–3177.

Müller, P., Holloway, G., Henyey, F. & Pomphrey, N. 1986 Nonlinear interactions among internal gravity waves. *Rev. Geophys.* **24**, 493–536.

Munk, W. H. 1981 A survey of internal waves and small scale processes. In *Evolution of Physical Oceanography* (ed. B. A. Warren & C. Wunsch), pp. 264–291. MIT Press.

Orlanski, I. & Cerasoli, C. P. 1981 Energy transfer among internal gravity modes: weak and strong interactions. *J. Geophys. Res.* C **86**, 4103–4124.

Phillips, O. M. 1966 *The Dynamics of the Upper Ocean*. Cambridge University Press.

Phillips, O. M. 1977 *The Dynamics of the Upper Ocean*, 2nd edn. Cambridge University Press.

Phillips, O. M. 1981 Wave interactions – the evolution of an idea. *J. Fluid Mech.* **106**, 215–227.

Pierrehumbert, R. T. 1986 Universal short-wave instability of two-dimensional eddies in an inviscid fluid. *Phys. Rev. Lett.* **57**, 2157–2159.

Schowalter, D. G., Van Atta, C. W. & Lasheras, J. C. 1994 A study of streamwise vortex structures in a stratified shear layer. *J. Fluid Mech.* **281**, 247–291.

Sonmor, L. J. & Klaassen, G. P. 1997 Toward a unified theory of gravity wave stability. *J. Atmos. Res.* **54**, 2655–2680.

Staquet, C. & Sommeria, J. 2002 Internal gravity waves: from instabilities to turbulence. *Annu. Rev. Fluid Mech.* **34**, 559–593.

Sutherland, B. 1999 Propagation and reflection of internal waves. *Phys. Fluids* **11**, 1081–1090.

Sutherland, B. 2000 Internal wave reflection in uniform shear. *Q. J. R. Met. Soc.* **126**, 3255–3287.

Sutherland, B. 2001 Finite-amplitude internal wavepacket dispersion and breaking. *J. Fluid Mech.* **429**, 343–380.

Teoh, S. G., Ivey, G. N. & Imberger, J. 1997 Laboratory study of the interaction between two internal wave rays. *J. Fluid Mech.* **336**, 91–122.

Thorpe, S. A. 1966 On wave interactions in stratified fluid. *J. Fluid Mech.* **24**, 737–751.

Thorpe, S. A. 1977 Turbulence and mixing in a Scottish loch. *Phil. Trans. R. Soc. Lond.* A **286**, 125–181.

Thorpe, S. A. 1994 The stability of statically unstable layers. *J. Fluid Mech.* **260**, 315–331.

Winters, K. B. & D'Asaro, E. A. 1994 Three-dimensional wave breaking near a critical level. *J. Fluid Mech.* **272**, 255–284.

Winters, K. B. & Riley, J. J. 1992 Instability of internal waves near a critical level. *Dyn. Atmos. Oceans* **16**, 249–278.